# Probing Flavor Structure of Cosmic Ray $e^{\mp}$ Spectrum and Implications for Indirect Dark Matter Searches

Shao-Feng Ge,$^{a,*}$   Hong-Jian He,$^{a,b,c,\dagger}$   Yu-Chen Wang,$^{b,d,\ddagger}$   Qiang Yuan $^{e,f,c,\S}$

$^a$ Tsung-Dao Lee Institute & School of Physics and Astronomy,
Shanghai Jiao Tong University, Shanghai 200240, China

$^b$ Institute of Modern Physics and Department of Physics,
Tsinghua University, Beijing 100084, China

$^c$ Center for High Energy Physics, Peking University, Beijing 100871, China

$^d$ Department of Physics, Harvard University, Cambridge, MA 02138, USA

$^e$ Key Laboratory of Dark Matter and Space Astronomy, Purple Mountain Observatory,
Chinese Academy of Sciences, Nanjing 210033, China

$^f$ School of Astronomy and Space Science,
University of Science and Technology of China, Hefei 230026, China

## Abstract

Measuring high energy cosmic ray electrons/positrons (CRE) provides important means for probing the nearby galactic sources and for the dark matter (DM) indirect detection. In this work, we perform a systematical analysis of the flavor structure of DM annihilations into charged leptons based on the cosmic ray CRE spectra measured by DAMPE, Fermi-LAT, AMS-02, and CALET experiments. We study the annihilations of possible TeV scale DM particles in a nearby subhalo, which is proposed to explain the possible peak-like structure of the DAMPE CRE data. We pay special attention to the possible non-resonant excess (besides the possible peak-like structure) and demonstrate that such non-resonant excess can mainly arise from the decay of muons produced by the DM annihilations in the subhalo. With these we study the flavor composition of the lepton final states of $\chi\chi \to e^+e^-$, $\mu^+\mu^-$, $\tau^+\tau^-$ by fitting the CRE data. We further analyze the constraints on the lepton flavor composition using the Fermi-LAT $\gamma$-ray measurements. We find that the flavor composition (favored by the CRE data) is consistent with the Fermi-LAT data at relatively low Galactic latitudes, while the fraction of the final state $\tau^{\pm}$ is severely bounded.

$^*$Email: gesf@sjtu.edu.cn
$^\dagger$Email: hjhe@sjtu.edu.cn, hjhe@tsinghua.edu.cn
$^\ddagger$Email: wang-yc15@mails.tsinghua.edu.cn
$^\S$Email: yuanq@pmo.ac.cn

# Contents

# 1. Introduction

High energy cosmic ray electrons and positrons (CRE) can provide important information about the nearby galactic sources [1] and the possible signals of dark matter (DM) annihilations or decays [2]. There have been very active experimental activities to measure the cosmic ray electron/positron spectrum up to TeV energy scale, including the ground-based and space-borne experiments such as HESS [3], VERITAS [4], Fermi-LAT [6], AMS-02 [5], and CALET [7]. Measuring the high energy CRE spectrum opens up an important window for the indirect detection of DM particles.

Among these experimental activities, the first announcement of the CRE energy spectrum measurement from $25\,\mathrm{GeV}$ up to $4.6\,\mathrm{TeV}$ [8] by the Dark Matter Particle Explorer (DAMPE) detector [9] provided some intriguing results. The DAMPE satellite was launched in December, 2015 and is optimized for detecting cosmic $e^{\pm}$ events and $\gamma$ rays up to about $10\,\mathrm{TeV}$ energy. The first CRE result of DAMPE collaboration was based on $530\,\mathrm{days}$ of data-taking [8]. The fitted CRE spectrum shows a spectral break around $0.9\,\mathrm{TeV}$ and is consistent with the HESS result [3]. The DAMPE CRE data also show a tentative peak-like event excess around $(1.3-1.5)\,\mathrm{TeV}$, which stimulated numerious studies on its possible interpretations [10]-[17], ranging from the conventional astrophysical sources (including pulsars and supernova remnants) to models of dark matter annihilations or decays into $e^{+}e^{-}$ events [18].

Our previous study [16] revealed a significant new hidden excess in the energy region $(0.6-1.1)\,\mathrm{TeV}$ on the left-hand-side of the peak bin $(1.3-1.5)\,\mathrm{TeV}$, and we proposed that this new excess originates from decays of the $1.5\,\mathrm{TeV}$ $\mu^{\pm}$ $(\tau^{\pm})$ events which are produced together with the $1.5\,\mathrm{TeV}$ $e^{\pm}$ peak events.

In this work, we perform a systematical analysis of the flavor structure of the CRE spectra and study their implications for indirect DM searches including the DAMPE, Fermi-LAT and CALET experiments. We make improved analysis with a physical CRE background, which is composed of the primary electrons produced by galactic supernova remnants (SNR) and the secondary electrons from the collision between primary nuclei and interstellar medium (ISM). We study annihilations of TeV scale DM particles into charged lepton pairs $(e^{+}e^{-},\,\mu^{+}\mu^{-},\,\tau^{+}\tau^{-})$ in a nearby subhalo. In addition to the possible peak-like structure measured by DAMPE, we pay special attention to the possible non-resonant excess mentioned above. We will show that the resultant CRE spectrum is consistent with the current CRE data of DAMPE and Fermi-LAT, and also the AMS-02 and CALET data. We demonstrate that including the muon decay channel not only improves the fitting quality, but also gives important constraint on the flavor structure of final state leptons from DM annihilations. We also take into account the photon radiation of the final state leptons, and derive nontrivial constraints on the flavor compositions of the final state leptons from the $\gamma$ ray measurements

of Fermi-LAT.

This paper is organized as follows. In Section 2, we first revisit our previous study [16], in which we fit the DAMPE data with a double-broken power-law background and with CRE signals from $\chi\chi \to e^+e^-, \mu^+\mu^-, \tau^+\tau^-$ channels. Then, we perform improved analysis with a physical CRE background and the CRE signal spectrum from DM annihilations in both $e^+e^-$ and $\mu^+\mu^-(\tau^+\tau^-)$ channels. With these we derive constraints on the flavor composition of the final state leptons from DM annihilations. We further estimate the increased sensitivities by the projected future DAMPE running. In Section 3, we fit the Fermi-LAT, AMS-02 and CALET data, and show the consistency with the $\mu^\pm$ ($\tau^\pm$) decay contribution invoked for explaining the DAMPE data. In Section 4, we further use the $\gamma$-ray measurement of Fermi-LAT to constrain the flavor composition of the final state leptons. Finally, we conclude in Section 5.

# 2. Improved Fit to the DAMPE CRE Spectrum

In our previous study [16], we used an empirical broken power-law formula to fit the background. In the present work, we will use a better justified CRE physical background instead and perform a more realistic analysis. In addition, we will allow the DM mass as a free parameter for the fit.

## 2.1. Fit with Broken Power-Law Background

In this subsection, we review what was done in Ref. [16], as a comparison with our new analysis in the current study. For clarity of our presentation, we replot in Fig. 1 all the DAMPE data points with $\pm 1\sigma$ errors [8]. From this, we observed [16] that the DAMPE data points exhibit another rather intriguing structure on the left-hand-side of the peak region $(1.3-1.5)$ TeV. We found that the energy range of $(0.616-1.07)$ TeV contains five consecutive data points (marked in red color), which all lie above the background curve (as fitted from the other background points marked in black color). These five red data points are distinctive and form a non-peak-like *new excess* with $\gtrsim 2\sigma$ significance.

In Ref. [16], an empirical broken power-law formula is adopted to describe the CRE backgrounds, without taking into account their origin (including the sources and the propagation effect). We first fit the background without including the five red data points over $(0.616-1.07)$ TeV and the blue peak point at $(1.3-1.5)$ TeV shown in Fig. 1. The fit gives a minimum $\chi^2$ per degree of freedom (d.o.f.), $\chi^2/\text{d.o.f} = 3.95/23 = 0.172$. We show the background fit as the black dashed curve in Fig. 1.

We then fit all the data points over the $25\,\text{GeV} - 2.6\,\text{TeV}$ region by adding the DM annihi-
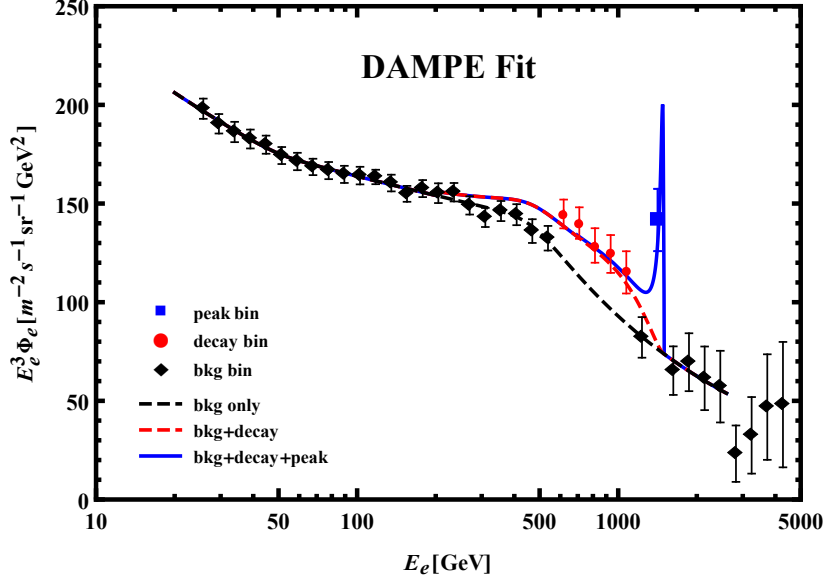
4

Figure 1: Fitting the CRE spectrum of DAMPE data. The fit of the background contribution is shown by the black dashed curve; the fit further including the decay contribution from $1.5\,\mathrm{TeV}$ $\mu^{\pm}$ ($\tau^{\pm}$) composition is depicted by the red dashed curve; and the fit further including $1.5\,\mathrm{TeV}$ $e^{\pm}$ peak-like contribution is given by the blue curve [16]. The DAMPE data [8] are shown by the dots with $\pm 1\sigma$ error bars.

lation contributions $\chi\chi \to e^{+}e^{-}$ and $\chi\chi \to \mu^{+}\mu^{-}(\tau^{+}\tau^{-}) \to e^{+}e^{-}$ to the background. For this analysis, we consider the DM particles with mass $M_{\chi} = 1.5\,\mathrm{TeV}$ and suppose that they are accumulated in a nearby DM subhalo whose density distribution is described by the generalized NFW profile [19], $\rho_{\chi}(r) \equiv \rho_{s}(r/r_{s})^{-\gamma}(1 + r/r_{s})^{\gamma-3}$, with $\rho_{s} = 100\,\mathrm{GeV/cm^{3}}$, $r_{s} = 0.1\,\mathrm{kpc}$, and $\gamma = 0.5$. We set the distance between the earth and the subhalo center as $d_{s} = 0.2\,\mathrm{kpc}$. For the CRE spectra at source, the annihilation channel $\chi\chi \to e^{+}e^{-}$ produces $e^{\pm}$ flux with exactly $1.5\,\mathrm{TeV}$ energy, while the energy spectrum of $e^{\pm}$ from $\chi\chi \to \mu^{+}\mu^{-}(\tau^{+}\tau^{-}) \to e^{+}e^{-}$ channels is given by

$$\frac{1}{N_{e}}\frac{\mathrm{d}N_{e}}{\mathrm{d}E_{e}} \simeq \frac{4}{M_{\chi}}\left(\frac{5}{12} - \frac{3E_{e}^{2}}{4M_{\chi}^{2}} + \frac{E_{e}^{3}}{3M_{\chi}^{3}}\right), \tag{2.1}$$

where the final states $e^{\pm}$ arise from the 3-body-decays $\mu \to e\bar{\nu}_{e}\nu_{\mu}$ or $\tau \to e\bar{\nu}_{e}\nu_{\tau}$. We note that $\mu$ and $\tau$ share almost the same decay spectra due to their energy $E = M_{\chi} \gg m_{\mu}, m_{\tau}$, except for their different decay branching fractions $\mathrm{Br}[\mu \to e\bar{\nu}_{e}\nu_{\mu}] \simeq 100\%$ and $\mathrm{Br}[\tau \to e\bar{\nu}_{e}\nu_{\tau}] \simeq 17.82\% \simeq 1/5.6$ [20]. The lifetime of flying $\mu^{\pm}$ with energy $E_{\mu} = 1.5\,\mathrm{TeV}$ is about 0.031s and could travel a distance about $9.36 \times 10^{6}\,\mathrm{m}$. The lifetime of $\tau^{\pm}$ is shorter than $\mu^{\pm}$ by another 7 orders of magnitude. Thus, the distances which $\mu^{\pm}$ and $\tau^{\pm}$ fluxes could travel before their decays are negligible as compared to $r_{s}$ and $d_{s}$. So we can treat the initial $e^{\pm}$ fluxes from all channels as produced at the source. For the flux propagating from the source $\mathbf{x}_{s}$ to a position

5

$\mathbf{x}$, it can be formulated as

$$\Phi_e(E_e) = \int \mathrm{d}^3 x_s \!\int \! \mathrm{d}E_s \, G(\mathbf{x}, E_e; \mathbf{x}_s, E_s) \, Q(\mathbf{x}_s, E_s) \,, \tag{2.2}$$

where $G(\mathbf{x}, E_e; \mathbf{x}_s, E_s)$ is the Green's function and $Q$ is the source function. (The propagation part will be further described in Section 2.3.) We fit the $e^\pm$ and $\mu^\pm$ ($\tau^\pm$) spectra together for the DAMPE data. This fit gives $\chi^2/\mathrm{d.o.f} = 16.5/27 = 0.609$, which has a better quality than any other naive fits (with the peak bin included).

From the above fit, we also derive the thermally averaged cross sections of the DM annihilations: $\langle \sigma v \rangle_e = 1.72 \times 10^{-26} \, \mathrm{cm}^3/\mathrm{s}$ and $\langle \sigma v \rangle_\mu + 0.178 \langle \sigma v \rangle_\tau = 1.47 \times 10^{-25} \, \mathrm{cm}^3/\mathrm{s}$. Their ratio (with $1\sigma$ bound) is given by $y = y_\mu + y_\tau = 8.6^{+1.4}_{-2.5}$, where $y_\mu = \langle \sigma v \rangle_\mu / \langle \sigma v \rangle_e$ and $y_\tau = 0.178 \langle \sigma v \rangle_\tau / \langle \sigma v \rangle_e$. We further deduce the 90% confidence limit (C.L.), $y = 2.6 - 10.8$. For lepton portal DM models [10, 21], we derive a non-trivial bound on the lepton-DM-mediator couplings $\lambda_j$ ($j = e, \mu, \tau$) [16],

$$\lambda_e : \left( \lambda_\mu^4 + \frac{1}{6} \lambda_\tau^4 \right)^{\frac{1}{4}} = 1 : y^{\frac{1}{4}} \,, \tag{2.3}$$

with a fairly narrow range $y^{\frac{1}{4}} \simeq 1.3 - 1.8$ (90% C.L.).

## 2.2. Physical Spectra for the CRE Backgrounds

In the previous subsection, we discussed fitting the CRE backgrounds with the empirical broken power-law formula as in Ref. [16]. For the current study, we will consider the physical components of the CRE backgrounds. The CRE backgrounds consist of the primary electrons from supernova remnants (SNR) and the secondary electrons/positrons produced by inelastic hadronic interactions of cosmic ray nuclei in the interstellar medium (ISM) [18]. They can be estimated numerically by the L$\textsc{ike}$DM code [22].

The primary electrons are considered to mainly arise from the SNR. Their injection spectrum can be formulated as [22],

$$\frac{\mathrm{d}N}{\mathrm{d}E_s} = A_e \left( \frac{E_s}{1\,\mathrm{GeV}} \right)^{-\gamma_2} \left[ 1 + \left( \frac{E_s}{E_{\mathrm{br}2}} \right)^2 \right]^{\frac{\gamma_2 - \gamma_3}{2}} \exp\left( -\frac{E_s}{E_{\mathrm{cut}}} \right), \tag{2.4}$$

for $E_s \gtrsim 20\,\mathrm{GeV}$. To estimate the primary electron background spectrum after propagation, we first approximate the injection spectrum with a series of Gaussian kernels,

$$\frac{dN}{dE_s} = \sum_{j=1}^{n} \frac{C_j}{\sqrt{2\pi}\,\sigma_j} \exp\left[ -\frac{(E_s - E_j)^2}{2\sigma_j^2} \right], \tag{2.5}$$

where $E_j = 0.01 \times 10^{(j-1)/7}\,\mathrm{GeV}$ and $\sigma_j = 0.15 E_j$ for $n = 50$ [22]. The post-propagation flux for each Gaussian kernel, $\Phi_i(E_e)$, is included in the L$\textsc{ike}$DM code. For the present analysis,

we will adopt its third set of the propagation parameters, in which the diffusion coefficient is parametrized as $D(x,E) = D_0(E/4\text{GeV})^\delta$ with $D_0 = 7.1 \times 10^{28} \text{cm}^2/\text{s}$ and $\delta = 0.33$ [22]. Thus, we obtain the total primary electron flux as a linear combination

$$\Phi(E_e) = \sum_{j=1}^{n} C_j \Phi_j(E_e) \,. \tag{2.6}$$

The secondary $e^+$ flux is computed according to the cosmic ray proton and Helium nuclei interactions with the ISM during their propagation. The secondary $e^-$ shares almost the same spectrum as the secondary $e^+$, but has an additional suppression factor of 0.6 [22]. This spectrum is also provided by the LikeDM code. Since the solar modulation effect is only significant in the low energy region $E < 10\,\text{GeV}$, it can be neglected in our fit.

## 2.3. CRE Spectra from DM Annihilations

We use the PPPC4DMID [23][24] package to calculate the electron spectra of the DM annihilation processes $\chi\chi \to e^+e^-$ and $\chi\chi \to \mu^+\mu^-(\tau^+\tau^-) \to e^+e^-$. The final state radiation (FSR) in the DM annihilation process will soften the CRE spectra. In Fig. 2(a), we show the injection spectra before and after FSR as dashed and solid curves, respectively. For clarity of presentation, we also rescaled the spectra of $\mu^\pm$ decay channel by an extra enhanecment factor of 50. Here we do not distinguish the spectra of $\mu^\pm$ and $\tau^\pm$ channels, since their shapes are rather similar except that the $\tau^\pm$ channel is suppressed by the much lower branching fraction of the 3-body-decays of $\tau^\pm$.

Next, we analyze the propagation of the $e^\pm$ flux from the nearby DM subhalo. When traveling across the interstellar space, CREs experience diffusion and energy loss, as described by the following propagation equation,

$$\frac{\partial N_e}{\partial t} - \frac{\partial[b(x,E)N_e]}{\partial E} - \nabla(D(x,E)\nabla N_e) = Q \,, \tag{2.7}$$

where $N_e(E_e, t, \mathbf{x})$ is the number density distribution as a function of the $e^\pm$ energy $E_e$ and the spacetime coordinates $(t, \mathbf{x})$.

The energy loss, $b(E) \equiv -\mathrm{d}E/\mathrm{d}t$, is defined as [23]:

$$b(x,E) = \frac{4\sigma_T}{3m_e^2} E^2 \left[ u_B(x) + \sum_i u_\gamma^{(i)}(x,E) \right], \tag{2.8}$$

where $u_B = \frac{1}{2}B^2$ stands for the energy density contribution from the galactic magnetic fields, and $u_\gamma^{(i)}$ is the energy density of photons from the CMB, starlight and dust-diffused infrared light. In the above equation, $\sigma_T = 8\pi\alpha_{\text{em}}^2/(3m_e^2)$ is the Thompson cross section. Since the size of the DM subhalo and its distance to earth are fairly small as compared to the galaxy size, we can ignore the $x$ dependence of $b$. Furthermore, at the location of solar system, which
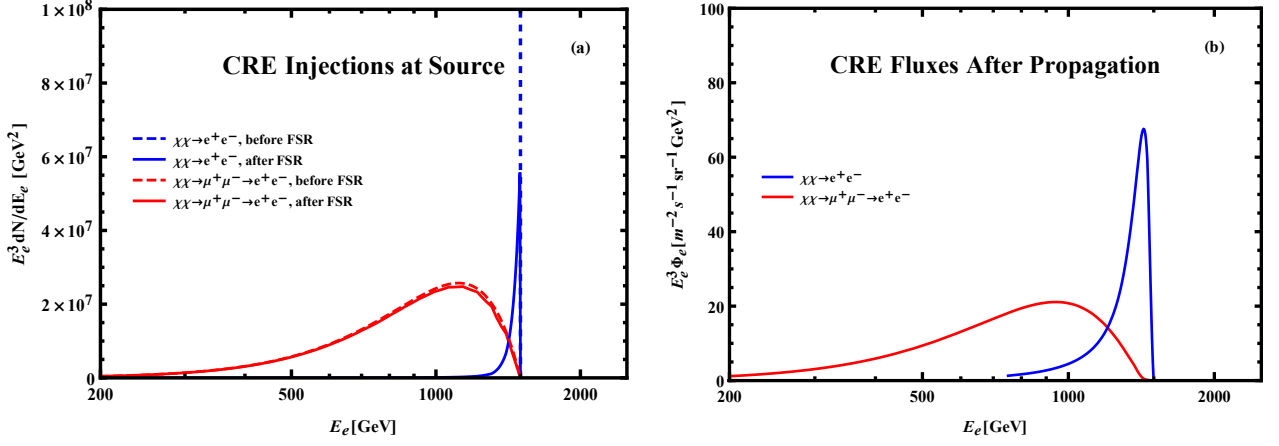
Figure 2: CRE energy spectrum at source and the fluxes after their propagation to the earth. Plot (a) presents the injection spectra of the CRE from DM annihilations. The blue curves show the $e^{\pm}$ channel and the red curves present the $\mu^{\pm}$ decay channel. The spectra after including the FSR are given by solid curves, while those without FSR are shown by dashed curves. For clarity, the spectra of $\mu^{\pm}$ decay channel is rescaled by an enhancement factor of 50. Plot (b) presents the CRE fluxes after the propagation to the earth. For illustration, the thermally averaged annihilation cross section of each channel is chosen as $\langle \sigma v \rangle_e = 2.0 \times 10^{-26}\,\mathrm{cm}^3/s$ and $\langle \sigma v \rangle_\mu = 1.5 \times 10^{-25}\,\mathrm{cm}^3/s$, while the DM mass is set as $M_\chi = 1.5\,\mathrm{TeV}$ for both plots.

is about $8\,\mathrm{kpc}$ away from our galaxy center, the galactic magnetic field is $B \sim 10^{-6}\,\mathrm{G}$, and hence $u_B$ is negligible. Thus, the energy-loss term can be rewriten as

$$b(x, E) = \frac{4\sigma_T \sum_i u_\gamma^{(i)}}{3m_e^2} E^2 = b_0 \left( \frac{E}{\mathrm{GeV}} \right)^2, \qquad (2.9)$$

with $b_0 = 10^{-16}\,\mathrm{GeV/s}$.

For the diffusion coefficient $D(x, E)$, we use the same parametrization as in Section 2.2. After conversion of units, we have

$$D(E) = 149 \left( \frac{E}{\mathrm{GeV}} \right)^{0.33} \mathrm{pc}^2/\mathrm{kyr}. \qquad (2.10)$$

The right-hand-side of Eq.(2.7) is the $e^{\pm}$ source function,

$$Q(\mathbf{x}, E_e) = C \frac{\langle \sigma v \rangle \rho_\chi^2(\mathbf{x})}{M_\chi^2} \frac{dN}{dE_e}, \qquad (2.11)$$

where $\rho_\chi(\mathbf{x})$ is the DM density distribution, $M_\chi$ is the mass of the DM particle, $\langle \sigma v \rangle$ is the thermally averaged annihilation cross section, and $dN/dE_e$ the $e^{\pm}$ is the energy spectrum from the DM annihilations. The coefficient $C = \frac{1}{4}$ for Dirac DM, and $C = \frac{1}{2}$ for Majorana DM [17]. For the current illustration, we will set $C = \frac{1}{4}$ hereafter. In this work, we use the generalized NFW density profile as in Ref. [16], $\rho_\chi(r) \equiv \rho_s (r/r_s)^{-\gamma} (1 + r/r_s)^{\gamma-3}$, with $\rho_s = 100\,\mathrm{GeV/cm}^3$, $r_s = 0.1\,\mathrm{kpc}$ and $\gamma = 0.5$. We set the distance between the earth and the

center of the subhalo as $d_s = 0.2\,\mathrm{kpc}$.

The propagation function (2.7) can be solved with the Green's function [25],

$$G(\mathbf{x}, E; \mathbf{x}_s, E_s) = \frac{\exp[-|\mathbf{x} - \mathbf{x}_s|^2/\lambda^2]}{b(E)(\pi\lambda^2)^{3/2}} \,, \tag{2.12}$$

where $E_s$ is the $e^{\pm}$ energy at source, and $E$ is the corresponding energy after propagation. The propagation scale $\lambda$ is given by

$$\lambda^2 = 4\int_E^{E_s} \mathrm{d}E' \frac{D(E')}{b(E')}. \tag{2.13}$$

Then, the solution of Eq.(2.7) can be expressed as

$$N_e(\mathbf{x}, E_e) = \int \mathrm{d}^3\mathbf{x}_s \int \mathrm{d}E_s G(\mathbf{x}, E_e; \mathbf{x}_s, E_s) Q(\mathbf{x}_s, E_s) \,. \tag{2.14}$$

Finally, the CRE flux $\Phi_e$ is related to the density distribution $N_e$ by

$$\Phi_e(\mathbf{x}, E_e) \equiv \frac{1}{4\pi} N_e(\mathbf{x}, E_e) v(E_e) \,, \tag{2.15}$$

where $v(E_e)$ is the velocity of electron with energy $E_e$. Since $E_e \gg m_e$ holds for the DAMPE data, we have $v \simeq c$. In Fig. 2(b), we plot the CRE flux from all channels after $e^{\pm}$ signals propagate to the earth. For illustration, we chose the thermally averaged annihilation cross section of each channel to be $\langle\sigma v\rangle_e = 2.0\times10^{-26}\mathrm{cm}^3/\mathrm{s}$ and $\langle\sigma v\rangle_\mu = 1.5\times10^{-25}\mathrm{cm}^3/\mathrm{s}$, and set the DM mass $M_\chi = 1.5\,\mathrm{TeV}$.

## 2.4. Fitting Event Excesses in CRE Spectrum

The total $e^{\pm}$ flux contains three parts, i.e., $\Phi_e \equiv \Phi_{\mathrm{bkg}} + \Phi_{\mathrm{decay}} + \Phi_{\mathrm{peak}}$, where the flux $\Phi_{\mathrm{bkg}}$ denotes the CRE backgrounds, $\Phi_{\mathrm{decay}}$ arises from the decay contributions of the $\mu^{\pm}(\tau^{\pm})$ as produced from the DM annihilations, and $\Phi_{\mathrm{peak}}$ is the contribution of $e^{\pm}$ as produced by the DM annihilations. We fit the DAMPE data points by minimizing the $\chi^2$ function,

$$\chi^2 = \sum_j \left[ \frac{1}{\sigma_j} \left( \Phi_j - \int_{E_j^l}^{E_j^u} \mathrm{d}E \, \frac{\Phi_e(E)}{E_j^u - E_j^l} \right) \right]^2 \tag{2.16}$$

where $\Phi_j$, $\sigma_j$, $E_j^l$ and $E_j^u$ stand for the detected CRE flux, the error, the lower and upper energy bounds of the $j$th bin, respectively.

Our best-fit result gives the DM mass $M_\chi = 1.54\,\mathrm{TeV}$, and the thermally averaged annihilation cross sections:

$$\langle\sigma v\rangle_e = 1.54\times10^{-26}\mathrm{cm}^3/\mathrm{s} \,, \tag{2.17a}$$

$$\langle\sigma v\rangle_{\mu\tau} = \langle\sigma v\rangle_\mu + 0.178\,\langle\sigma v\rangle_\tau = 1.39\times10^{-25}\mathrm{cm}^3/\mathrm{s} \,. \tag{2.17b}$$
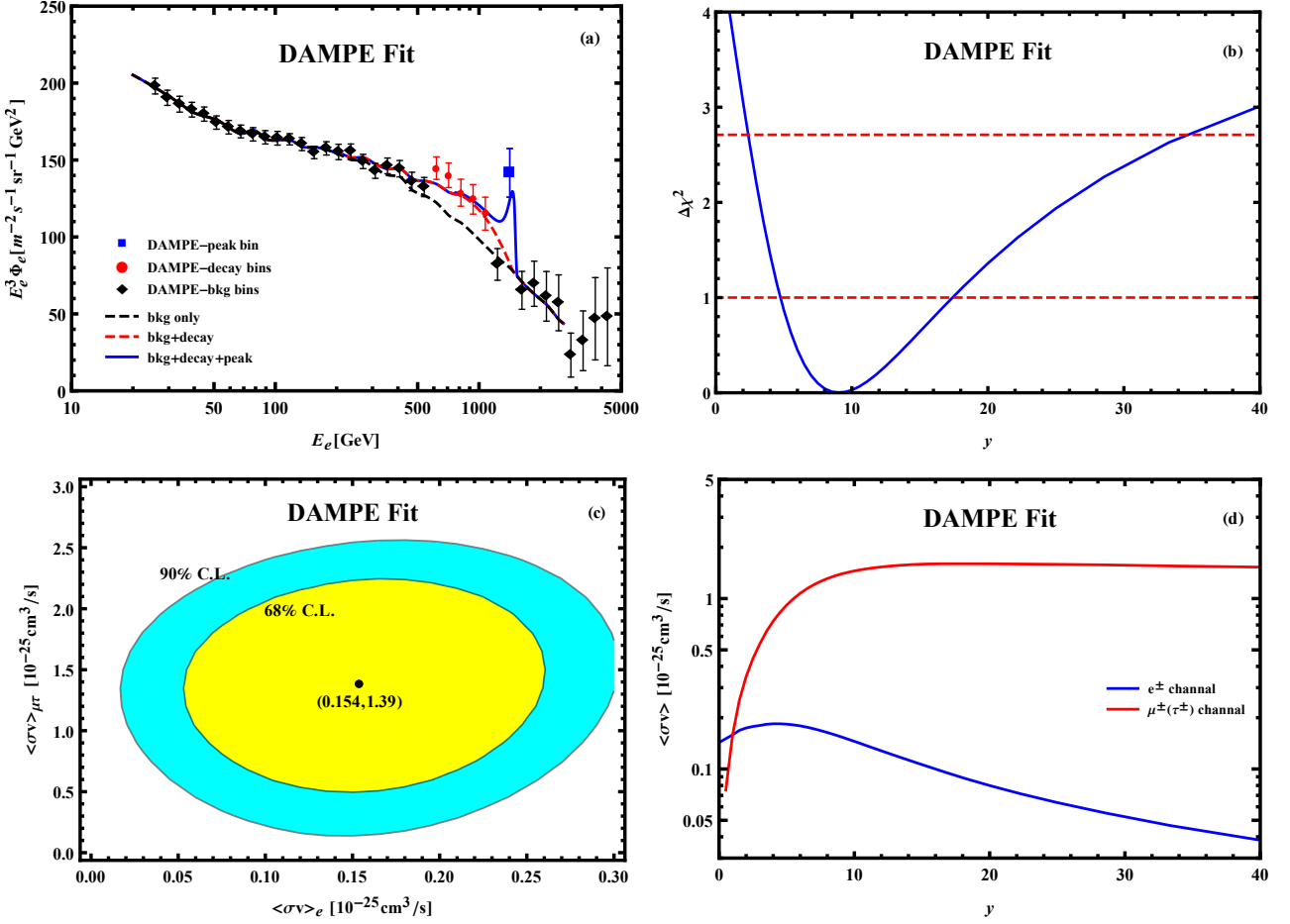
9

Figure 3: Plot (a): Improved fit for the DAMPE CRE spectrum, with the central value of the flavor ratio $y = 9.0$. Plot (b): $\Delta\chi^2$ as a function of the flavor ratio $y$. The allowed ranges of the flavor ratio are $y = 9.0^{+8.4}_{-4.2}$ (1$\sigma$) and $2.4 < y < 34.7$ (90% C.L.). Plot (c): $\Delta\chi^2$ contours for the DM annihilation cross sections of $e^{\pm}$ versus $\mu^{\pm}(\tau^{\pm})$ channels. The $\mu^{\pm}(\tau^{\pm})$ decay contribution is nonzero at 90% C.L. Plot (d): The cross sections $\langle\sigma v\rangle_e$ and $\langle\sigma v\rangle_{\mu\tau}$ as functions of the flavor ratio $y$.

The ratio of cross sections between the final state $\mu^{\pm}(\tau^{\pm})$ and the final state $e^{\pm}$ is given by $y = y_\mu + y_\tau \simeq 9.0$, with $y_\mu = \langle\sigma v\rangle_\mu / \langle\sigma v\rangle_e$ and $y_\tau = 0.178\,\langle\sigma v\rangle_\tau / \langle\sigma v\rangle_e$. For the CRE background spectrum (2.4), this fit gives the following parameters:

$$A_e = 0.130\,\text{GeV}^{-1}, \quad \gamma_2 = 2.80, \quad \gamma_3 = 2.29, \quad E_{\text{br2}} = 46.3\,\text{GeV}, \quad E_{\text{cut}} = 2.56\,\text{TeV}. \qquad (2.18)$$

The fitting quality is given by $\chi^2/\text{d.o.f.} = 19.6/26 = 0.756$, which is fairly good. We note that the largest deviation between the data and our model comes from the $(1.1-1.3)\,\text{TeV}$ bin in Fig. 3(a), i.e., the black bin lying between the red bins and the blue peak bin, which is $2.8\sigma$ below the best fit value in the blue curve. This contributes about 40% of the total $\chi^2$ value.

We present our new fit of the CRE spectrum including the $\mu^{\pm}(\tau^{\pm})$ decay contribution (red curve) and the peak signal (blue curve) in Fig. 3(a). Impressively, this demonstrates that including the $\mu^{\pm}(\tau^{\pm})$ decay events can fully explain this non-peak-like new excess over the

| Varying Peak Signals | $\langle\sigma v\rangle_e$ ($10^{-25}$cm$^3$/s) | $\langle\sigma v\rangle_{\mu\tau}$ ($10^{-25}$cm$^3$/s) | Flavor Ratio $y$ |
|---|---|---|---|
| original value | 0.154 | 1.39 | 9.0 |
| $+1\sigma$ upper value | 0.215 | 1.30 | 6.1 |
| $-1\sigma$ lower value | 0.094 | 1.47 | 15.7 |

Table 1: Fluctuation of the peak signals versus the contribution of $\mu^\pm$ ($\tau^\pm$) channel. When the number of peak signal events fluctuates within $\pm 1\sigma$ range, the contribution of the $e^\pm$ channel varies accordingly (2nd column), but the contribution of $\mu^\pm$ ($\tau^\pm$) channel (3rd column) only changes by less than 6% and remains nearly the same in the fit. The last column shows that the corresponding change of the flavor ratio $y$ is mainly due to the fluctuation of peak signals.

$(0.6 - 1.1)\,\text{TeV}$ energy region.

We can derive the constraints on the flavor ratio $y$ through marginalization. We scan the value of $y$ in a wide range, and compute the $\Delta\chi^2$ as a function of $y$. This is plotted as the blue curve in Fig. 3(b). We find that the flavor ratio with $1\sigma$ bounds is $y = 9.0^{+8.4}_{-4.2}$, and its 90% confidence limits are $2.4 < y < 34.7$.[1] If we set $y = 0$, the best fit has its $\chi^2$ value increase to $\chi^2/\text{d.o.f.} = 24.7/27 = 0.914$. For this case, the minimal $\chi^2$ increases by $\Delta\chi^2 = 5.02$, in which the 5 non-resonant red bins contribute $\Delta\chi^2 = 4.68$. This shows that including the $\mu^\pm$ ($\tau^\pm$) decay contribution ($y > 0$) for fitting the 5 red bins does play an important role to improve the fitting quality.

In Fig. 3(c), we marginalize the two cross sections, $\langle\sigma v\rangle_e$ and $\langle\sigma v\rangle_{\mu\tau} = \langle\sigma v\rangle_\mu + 0.178\,\langle\sigma v\rangle_\tau$, which determines the final state $e^\pm$ events from the 3-body decays of the final states $\mu^\pm$ and $\tau^\pm$. We show their 68% and 90% confidence limits as the yellow and light blue contours, respectively. Our fit demonstrates that a nonzero $\mu^\pm$ ($\tau^\pm$) decay contribution is required at 90% C.L.

We also note that in Fig. 3(c), the shapes of the $\Delta\chi^2$ contours are close to ellipses with two axes nearly parallel to the horizontal/vertical directions, which means that the statistical correlation between the cross sections is quite weak. This fact means that these two parameters may be fitted independently. We illustrate this point in Table 1. Here we fluctuate the number of peak signal events by $\pm 1\sigma$ and find that although the contribution of $e^\pm$ channel varies accordingly (2nd column), the contribution of $\mu^\pm$ ($\tau^\pm$) channel only changes by less than 6% (3rd column) and remains nearly the same in the fit. Then, we note that the flavor ratio $y$ (4th column) has significant changes mainly due to the fluctuation of peak signals. It shows that even if the annihilation rate to the $e^\pm$ channel and hence the value of the flavor ratio $y$ may change significantly, the contribution from the non-resonant $\mu^\pm$ ($\tau^\pm$) channel is largely

---

[1]This improved analysis differs from our previous fit [16], where we made a separate background fit, and then with the background parameter $E_{\text{br2}}$ varying within its 90% limits we further fitted the signal contributions. In the current analysis, we fit the background parameters and signal parameters simultaneously, so it gives weaker but more reasonable limits.

independent of the event number in the peak bin and fairly robust. Finally, we note that the small change of the cross section $\langle\sigma v\rangle_{\mu\tau} [= \langle\sigma v\rangle_\mu + 0.178 \langle\sigma v\rangle_\tau]$ in the above fit mainly comes from the tension in the non-resonant bin of $(1.1-1.3)\,\mathrm{TeV}$ (which is on the left-hand-side of the peak bin). Namely, in Fig. 3(a) we see that this $(1.1-1.3)\,\mathrm{TeV}$ bin is significantly below the blue curve; so reducing events in the peak bin will slightly soften the tension with this bin and thus allow more $\mu^\pm\,(\tau^\pm)$ contribution. From the above analysis, we find that *the evidence of the non-peak excess can stand by itself, and is fairly independent of the peak excess.*

When making the $\chi^2$ fit in Fig. 3(b) for each given $y$ value, we also obtain the fit values for other free parameters as functions of $y$, including the two cross sections. We explicitly plot the two fitted cross sections in Fig. 3(d). From these curves, we observe that for $y = y_\mu + y_\tau \gtrsim 9$ the $\mu^\pm\,(\tau^\pm)$ decay contribution remains fairly flat, and the cross section $\langle\sigma v\rangle_e$ drops roughly as $y^{-1}$. This means that for larger values of $y$, the contribution from $\mu^\pm\,(\tau^\pm)$ decays is already maximized, so the increase of $y$ is mainly caused by the decrease of the $e^\pm$ cross section $\langle\sigma v\rangle_e$. The fact that the contribution of $e^\pm$ channel gets suppressed for large $y$ is important for our $\gamma$ ray analysis, which will be discussed in Section 4.

## 2.5. Origin of Flavor Composition of CRE Spectrum

From the analysis in Section 2.4, we find that the original lepton final state produced at a nearby source should have a flavor composition ratio, $N_e : (N_\mu + 0.178 N_\tau) = 1 : y$, with the constrained range $2.4 < y < 34.7$ at $90\%$ C.L. (Our analysis here used the current improved fit of $y$ which differs from our previous analysis [16] and is more reliable.) We note that in the above ratio, the $\tau$ component could only play a minor role due to the suppression by its small decay branching fraction $\mathrm{Br}[\tau \to e\,\bar\nu_e\nu_\tau] \simeq 17.82\%$. The simplest realization of this flavor composition condition is $N_e : N_\mu : N_\tau \approx 1 : y : 0$, where all the non-peak excesses are given by the decay contribution of muon flavor.

The above flavor composition condition will place important constraint on the lepton-related DM model building. For instance, we can consider the typical lepton portal DM models [10, 21], where the DM particle is either a fermion or scalar. For the case of fermionic DM, consider a neutral singlet Dirac fermion $\chi$ as the DM, which interacts with a scalar mediator $S$ and the right-handed charged lepton $\ell_{Rj}$,

$$\mathcal{L}_\chi \supset \lambda_j S_j \,\overline{\chi}\ell_j + \mathrm{h.c.} \tag{2.19}$$

where $\ell_j = e, \mu, \tau$. For the case of scalar DM, consider a neutral complex singlet scalar $X$ as the DM particle and a Dirac fermion $\psi$ as the mediator (which has the same electric charge and lepton number as the charged leptons). The relevant interaction Lagrangian is given by

$$\mathcal{L}_X \supset \lambda_j X \overline{\psi_j}\ell_j + \mathrm{h.c.} \tag{2.20}$$

The above interactions will realize the DM annihilation process $\chi\bar{\chi} \to \ell_j\ell_j$ or $XX \to \ell_j\ell_j$ via the $t$-channel exchange of $S_j$ or $\psi_{Lj}$. We note that the cross section of DM annihilations is proportional to $\lambda_j^4$. For the above simplest realization of the flavor composition condition, we can deduce $N_e : N_\mu : N_\tau = \lambda_e^4 : \lambda_\mu^4 : \lambda_\tau^4 = 1 : y : 0$, where the flavor ratio $y$ is constrained within $2.4 < y < 34.7$ at 90% C.L. Hence, this results in a simple coupling relation, $\lambda_e : \lambda_\mu : \lambda_\tau = 1 : y^{\frac{1}{4}} : 0$, with $y^{\frac{1}{4}} \simeq 1.2 - 2.4$. In general, including the possible decay contribution of $\tau$ leptons, we infer the following condition for DM couplings,

$$\lambda_e : \left(\lambda_\mu^4 + \frac{1}{6}\lambda_\tau^4\right)^{\frac{1}{4}} = 1 : y^{\frac{1}{4}}. \tag{2.21}$$

where the flavor ratio $y$ is confined into a rather narrow range $y^{\frac{1}{4}} \simeq 1.2 - 2.4$ (90% C.L.). We may consider that the lepton-DM portal sector poses a $\mu - \tau$ flavor symmetry and thus realizes $\lambda_\mu = \lambda_\tau$. Then, we can use this to derive a neat coupling relation from Eq.(2.21),

$$\lambda_e : \lambda_\mu : \lambda_\tau = 1 : \tilde{y}^{\frac{1}{4}} : \tilde{y}^{\frac{1}{4}}, \tag{2.22}$$

with $\tilde{y}^{\frac{1}{4}} = \left(\frac{6}{7}y\right)^{\frac{1}{4}} \simeq 1.2 - 2.3$. This constraint provides important guideline for the DM model buildings. It is encouraging to further apply this analysis for testing DM interactions with leptons.

## 2.6. Impacts of DAMPE Future Running

Up to the end of 2019, the DAMPE satellite had accumulated data for 4 years, and is expected to run up to 6 years or even longer. As the data size grows, the statistical errors will decrease. Assuming the same central values of the detected CRE fluxes, the statistical errors will scale with time as $\sigma_{\text{stat}} \propto t^{-1/2}$. This means that the statistical errors of the 4-year data is reduced to $\sqrt{1.5/4} \simeq 61\%$ of that of the released data in 2017 [8], and the 6-year measurements will reduce the statistical errors to $\sqrt{1.5/6} = 50\%$. We assume that the same systematical errors as before.

We redo the fit for the projected 6-year data taking of DAMPE, and present the results in Fig. 4(a). This new fit gives

$$A_e = 0.106\,\text{GeV}^{-1}, \quad \gamma_2 = 2.73, \quad \gamma_3 = 2.27, \quad E_{\text{br2}} = 57\,\text{GeV}, \quad E_{\text{cut}} = 2.46\,\text{TeV}, \tag{2.23}$$

for the background parameters, together with the DM mass $M_\chi = 1.54\,\text{TeV}$, and the DM annihilation cross sections $\langle\sigma v\rangle_e = 1.52 \times 10^{-26}\text{cm}^3/\text{s}$ and $\langle\sigma v\rangle_{\mu\tau} = 1.22 \times 10^{-25}\text{cm}^3/\text{s}$. For the fitting quality, we have $\chi^2/\text{d.o.f.} = 51.6/26 = 1.98$. The increased $\chi^2$ value of this fit is mainly due to the reduction of the statistical errors of the 6-year data taking. The $\Delta\chi^2$ as a function of the flavor ratio $y$ is plotted in Fig. 4(b). We obtain the flavor ratio $y = 8.0^{+3.9}_{-3.0}$ (1$\sigma$) and $3.4 < y < 15.7$ at 90% C.L. For the case of $y = 0$, we find that $\chi^2$ increases by
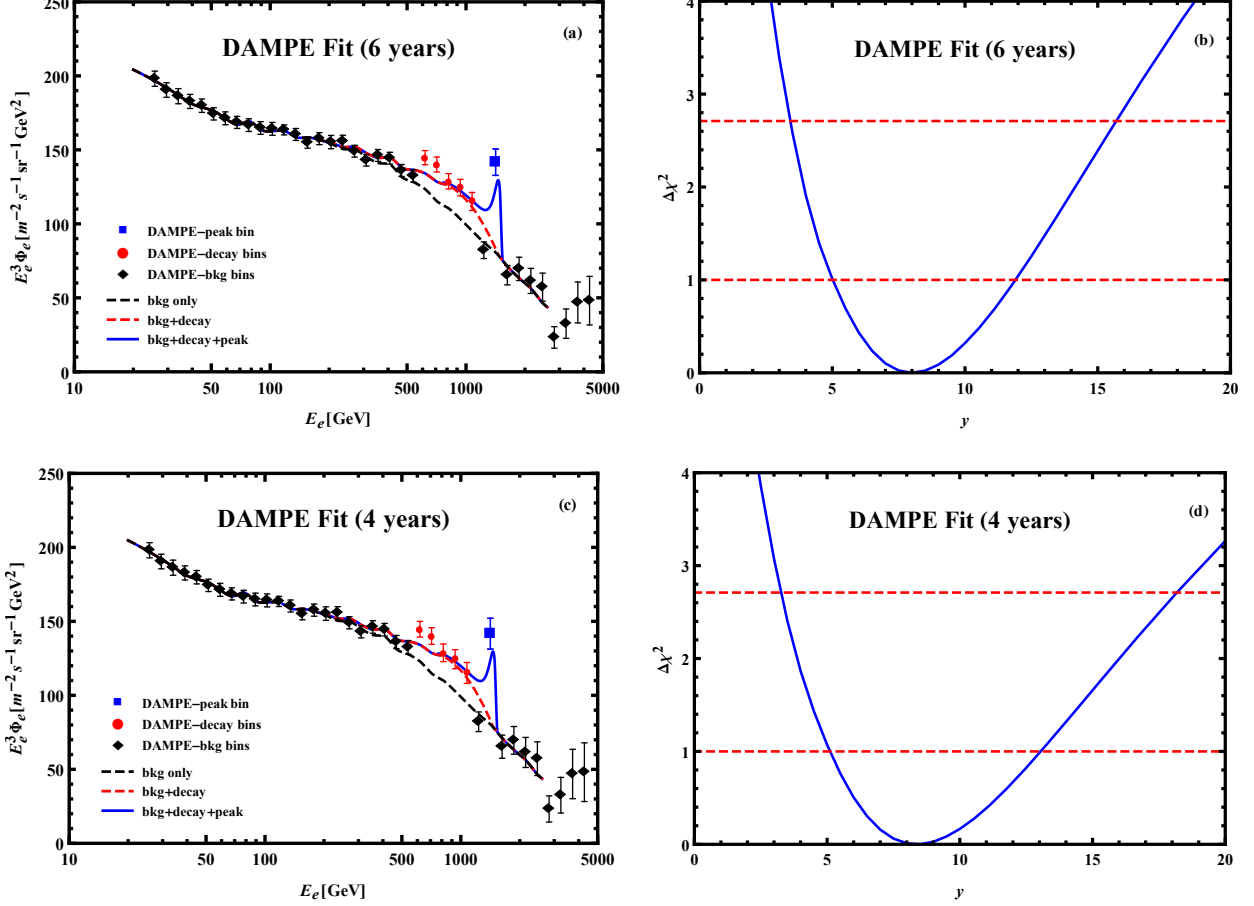
Figure 4: Fits of DAMPE CRE spectra for projected 4-year and 6-year data taking. Plot (a): Fitting the DAMPE data with the projected 6-year data taking, which reduces the current statistical errors by 50%. (Accordingly, the error bars are smaller than those in Fig. 3(a) by about a factor of $1/2$ at high energies.) Plot (b): Marginalization of $y$ for the projected 6-year data taking of DAMPE, which gives the constraints on the flavor ratio $y = 8.0^{+3.9}_{-3.0}$ $(1\sigma)$ and $3.4 < y < 15.7$ $(90\%\,\text{C.L.})$. Plot (c): Fitting the DAMPE data with the projected 4-year data taking. Plot-(d): Marginalization of $y$ for the projected 4-year data taking of DAMPE, which gives the bounds $y = 8.4^{+4.6}_{-3.3}$ $(1\sigma)$ and $3.3 < y < 18.2$ $(90\%\,\text{C.L.})$.

$\Delta\chi^2 = \chi^2(y=0) - \chi^2_{\text{min}} = 11.1$, in which the 5 red bins provide $\Delta\chi^2 = 12.4$ as the dominant contribution. The reason why the total increase $\Delta\chi^2$ is less than the contribution from the 5 red bins is because in certain bins the changes in $\Delta\chi^2$ are negative.

For comparison, we apply the same analysis to the projected 4-year DAMPE data. We present the results in Fig. 4(c)-(d). This fit gives the DM mass $M_\chi = 1.54\,\text{TeV}$, and annihilation cross sections $\langle\sigma v\rangle_{\mu\tau} = 1.28 \times 10^{-25}\text{cm}^3/\text{s}$ and $\langle\sigma v\rangle_e = 1.53 \times 10^{-26}\text{cm}^3/\text{s}$. From Fig. 4(d), we derive bounds on the flavor ratio, as $y = 8.4^{+4.6}_{-3.3}$ at $1\sigma$ level and $3.3 < y < 18.2$ at $90\%$ C.L. This fit also gives corresponding background parameters,

$$A_e = 0.116\,\text{GeV}^{-1}, \quad \gamma_2 = 2.76, \quad \gamma_3 = 2.28, \quad E_{\text{br2}} = 52\,\text{GeV}, \quad E_{\text{cut}} = 2.50\,\text{TeV}. \tag{2.24}$$

It has the fitting quality $\chi^2/\text{d.o.f.} = 39.6/26 = 1.52$.

# 3. Comparison with Other CRE Detections

In this section, we will extend our analysis of Section 2 to further combine the CRE measurement of Fermi-LAT [6] in Section 3.1, and then compare it with the recent data from AMS-02 [5] and CALET [7] in Section 3.2.

## 3.1. Combined Fit with Fermi-LAT

We note that the CRE measurement by Fermi-LAT [6] shows good consistency with the DAMPE result [8] even for the high energy region. We observe that the CRE spectrum of Fermi-LAT exhibits a rise around $(0.6-1.2)\,\mathrm{TeV}$ region, which is consistent with the non-resonant excess (5 red bins) of the DAMPE result in Fig. 1, and thus may hint the $\mu^{\pm}$ ($\tau^{\pm}$) decay signals. Although the Fermi-LAT data do not show a clear peak-like signal around $(1.3-1.5)\,\mathrm{TeV}$ (unlike DAMPE), this is still consistent because the energy resolution of Fermi-LAT is about $(10-20)\%$ [6] above $1\,\mathrm{TeV}$ energy scale, and is much larger than the DAMPE energy resolution $(1-2)\%$ [8, 9].

In the following, we will make a combined fit for both the DAMPE data $(25\,\mathrm{GeV}-2.6\,\mathrm{TeV})$ and the Fermi-LAT data with the high energy (HE) selection $(42\,\mathrm{GeV}-2.1\,\mathrm{TeV})$. For this, we define the total $\chi^2$ as follows,

$$
\begin{aligned}
\chi^2 &= \chi^2(\text{DAMPE}) + \chi^2(\text{Fermi-LAT}) \\
&= \sum_j \left[ \frac{1}{\sigma_j^{\mathrm{D}}} \left( \Phi_j^{\mathrm{D}} - \int_{E_j^{l\mathrm{D}}}^{E_j^{u\mathrm{D}}} \frac{\Phi_e^{\mathrm{D}}(E)}{E_j^{u\mathrm{D}} - E_j^{l\mathrm{D}}} \, \mathrm{d}E \right) \right]^2 + (\mathrm{D} \leftrightarrow \mathrm{F}) \,,
\end{aligned} \tag{3.1}
$$

where the superscript D (F) stands for DAMPE (Fermi-LAT), and the quantities $E_j$, $E_j^l$, $E_j^u$, $\sigma_j$ and $\Phi_j$ are the same as those defined in Eq.(2.16).

The DAMPE detector has high energy resolution of $(1-2)\%$ [8, 9], so we have $\Phi_e^{\mathrm{D}} \simeq \Phi_e$ for DAMPE data, where $\Phi_e$ is the original CRE flux spectrum. But for Fermi-LAT data, because the energy resolution is much lower than DAMPE, we should take it into account for the measured flux $\Phi_e^{\mathrm{F}}$. The energy resolution can be described by a Gaussian distribution. For the Fermi-LAT data, we convolve $\Phi_e$ with this Gaussian distribution through the integral,

$$
\Phi_e^{\mathrm{F}}(E^{\mathrm{F}}) \equiv \int \Phi_e(E) \frac{1}{\sqrt{2\pi}\Delta_E} \exp\left[ -\frac{(E^{\mathrm{F}}-E)^2}{2\Delta_E^2} \right] \mathrm{d}E \,, \tag{3.2}
$$

where $\Delta_E$ is the energy resolution at a given energy $E$. The specific values of $\Delta_E$ (as a function of $E$) are adopted from Fig. 10 of Ref. [6].

We fit the DAMPE data and Fermi-LAT data by minimizing the combined $\chi^2$. The quality of the best fit is $\chi^2/\mathrm{d.o.f.} = 61.0/53 \simeq 1.15$. The fit gives the background parameters,

$$
A_e = 0.762\,\mathrm{GeV}^{-1}, \quad \gamma_2 = 3.42, \quad \gamma_3 = 2.28, \quad E_{\mathrm{br2}} = 28\,\mathrm{GeV}, \quad E_{\mathrm{cut}} = 3.09\,\mathrm{TeV}, \tag{3.3}
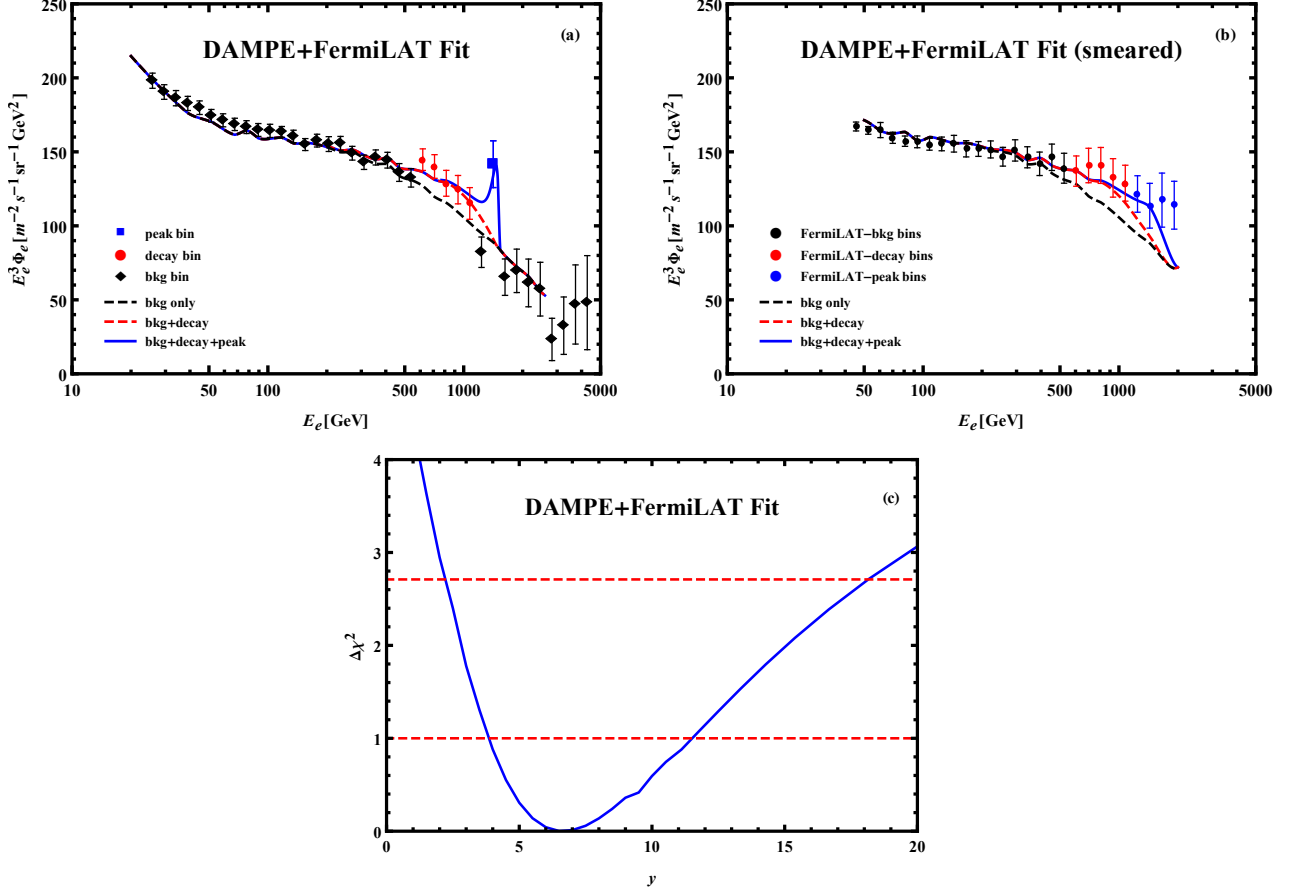$$

Figure 5: Combined fit of CRE energy spectra for both DAMPE and Fermi-LAT data. Plot (a): The best-fit result is compared with the DAMPE data points (with error bars). Plot (b): The same best-fit result is convolved with Fermi-LAT's energy resolution (marked as "smeared"), and is compared with the Fermi-LAT data points (with error bars). Plot (c): The $\Delta\chi^2$ values versus $y$ from our fit, which gives $y = 6.6^{+4.9}_{-2.8}$ at $1\sigma$ and $2.2 < y < 18.1$ at 90% C.L.

as well as the DM mass $M_\chi = 1.54\,\mathrm{TeV}$, and annihilation cross sections $\langle\sigma v\rangle_{\mu\tau} = 1.07 \times 10^{-25}\mathrm{cm}^3/\mathrm{s}$ and $\langle\sigma v\rangle_e = 1.61\times10^{-26}\mathrm{cm}^3/\mathrm{s}$. In Fig. 5, we present our fit of both fluxes $\Phi^\mathrm{D}$ (for DAMPE data) and $\Phi^\mathrm{F}$ (for Fermi-LAT data) in the plots (a) and (b), respectively. These arise from the same fit, but due to the convolution with the energy resolution of Fermi-LAT, the shape of the curve of $\Phi^\mathrm{F}$ [plot (b)] is not identical to that of $\Phi^\mathrm{D}$ [plot (a)].

Furthermore, we plot $\Delta\chi^2$ as a function the flavor ratio $y$ in Fig. 5(c). From this, we derive the $1\sigma$ bound on the flavor ratio $y = 6.6^{+4.9}_{-2.8}$, and the 90% C.L. bound, $2.2 < y < 18.1$. We note that the case of $y = 0$ worsens the fit quality considerably, with the $\chi^2$ value increasing by 5.9. This indicates again that including the $\mu^\pm(\tau^\pm)$ decay contribution is favored by the combined data of DAMPE and Fermi-LAT.

Finally, for comparison, we summarize in Table 2 our fits of the CRE energy spectra for the current DAMPE data, the projected 4-year and 6-year running of DAMPE, and the combined data set of DAMPE+Fermi-LAT.

| Experiments | $\chi^2$/d.o.f | $M_\chi$ (TeV) | $\langle\sigma v\rangle_e$ | $\langle\sigma v\rangle_{\mu\tau}$ | $y$ |
|---|---|---|---|---|---|
| DAMPE | 19.6/26=0.756 | 1.54 | 0.154 | 1.39 | $9.0^{+8.4}_{-4.2}$ |
| DAMPE (in 4y) | 39.6/26=1.52 | 1.54 | 0.153 | 1.28 | $8.4^{+4.6}_{-3.3}$ |
| DAMPE (in 6y) | 51.6/26=1.98 | 1.54 | 0.152 | 1.22 | $8.0^{+3.9}_{-3.0}$ |
| DAMPE+Fermi-LAT | 61.0/53=1.15 | 1.54 | 0.161 | 1.07 | $6.6^{+4.9}_{-2.8}$ |

Table 2: Comparison of the fitting results for DAMPE and Fermi-LAT experiments. The second row presents our fit of the current DAMPE data, the third (fourth) row shows the fit for the projected 4-year (6-year) data taking of DAMPE, and the fifth row gives our combined fit of the current DAMPE and Fermi-LAT data. The fourth and fifth columns summarize the best fits of DM annihilation cross sections via $e^\pm$ and $\mu^\pm (\tau^\pm)$ channels, respectively (in the unit of $10^{-25}$cm$^3$/s). The last column shows the central value and the $1\sigma$ bounds of the flavor ratio $y = \langle\sigma v\rangle_{\mu\tau}/\langle\sigma v\rangle_e$.

## 3.2. Comparison with AMS-02 and CALET

In this subsection, we will further compare our DAMPE analysis (Section 2) with the AMS-02 and CALET data.

The CALET collaboration gave a recent update of its CRE measurement over the energy range $(0.011-4.8)$TeV in June, 2018 [7]. The CRE spectrum of CALET is consistent with a break at 0.9 TeV (as found by the DAMPE observation [8]). The CALET data do not show a peak structure around $(1.3-1.5)$ TeV, but it is premature to draw any firm conclusion since CALET still has sizable statistical uncertainties beyond 1 TeV energy. The AMS collaboration published new precision measurements of cosmic ray electrons up to 1.4 TeV in March, 2019 [5]. Together with their positron measurement published in January, 2019, the CRE spectrum of AMS-02 shows agreement with the CALET result [7] up to 1 TeV. However, this measurement does not reach the energy region of the peak excess shown by DAMPE data. We can hardly compare the non-peak excess of DAMPE with the AMS-02 result as well, because the latter only shows two data points over the energy region $(0.6 - 1.1)$ TeV.

In view of the current situation discussed above, we need not to fit all the DM parameters with the AMS-02 and CALET data in this subsection. Instead, we will just test a few benchmark cases motivated by our analysis in Section 2.4. We combine the CALET data (using the same energy binning as DAMPE analysis) with the AMS-02 data (electron + positron), and apply the $\chi^2$ fit to the following three cases:
(a). There is only background CRE flux without assuming any $e^\pm$ signals from the DM annihilation.
(b). There exist $e^\pm$ signals from the DM annihilations, with the DM mass $M_\chi = 1.535$ TeV, the annihilation cross section $\langle\sigma v\rangle_e = 1.54 \times 10^{-26}$cm$^3$/s and the flavor ratio $y = 9.0$ as given by the best fit of Section 2.4.
(c). Same as Case-(b), but the DM mass is allowed to vary within the range $M_\chi \in [1.7, 1.9]$ TeV.
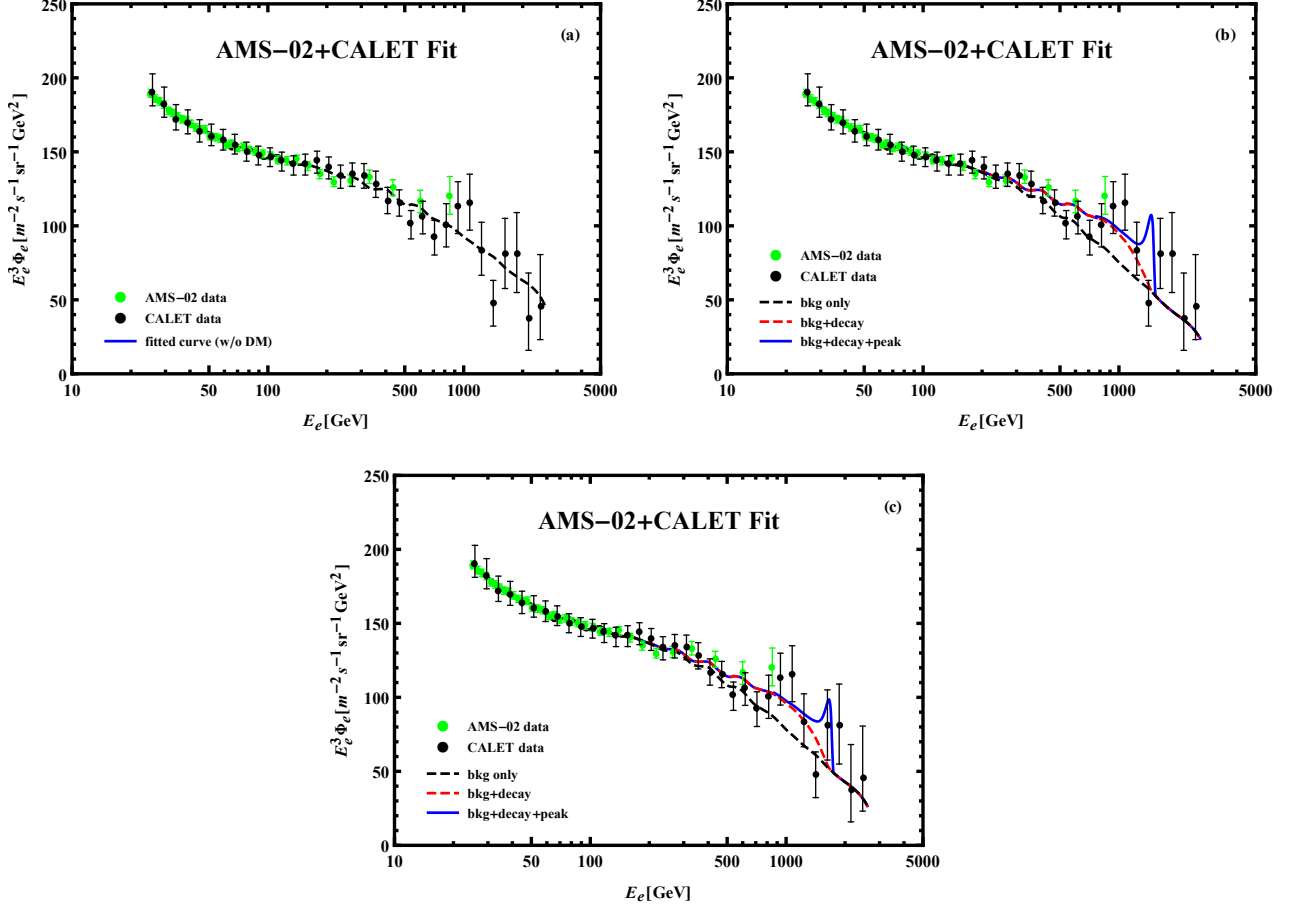
Figure 6: Combined fit of the CRE energy spectra from AMS-02 and CALET. In each plot, the AMS-02 (CALET) data are shown as green (black) dots, including their $1\sigma$ error bars. Plot (a): The best fit without DM contribution, defined as Case-(a) in the text, with $\chi^2/\text{d.o.f.} = 36.32/64 = 0.567$. Plot (b): The best fit of CALET in Case-(b) with $\chi^2/\text{d.o.f.} = 43.95/61 = 0.721$, where we input the best-fit of the flavor ratio $y$ from DAMPE data as in Section 2.4. Plot (c): The best fit of Case-(c) which includes the DM mass for fit and gives $M_\chi = 1.745\,\text{TeV}$. The corresponding fit quality, $\chi^2/\text{d.o.f.} = 37.39/61 = 0.613$, is comparable to Case-(a).

For the above three cases, our fits have the fit quality

$$\chi^2/\text{d.o.f.} = (36.32/64,\ 43.95/61,\ 37.39/61) \simeq (0.567,\ 0.721,\ 0.613), \tag{3.4}$$

respectively. Also, the fit of Case-(c) gives the DM mass $M_\chi = 1.745\,\text{TeV}$. We see that adding the dark matter contribution does not affect much the fitting quality. We present the fitted CRE energy spectra for the three cases in plots (a)-(c) of Fig. 6.

Inspecting the CALET CRE spectrum alone, we note that there apppear two broad excesses around the windows $(0.75-1.2)\,\text{TeV}$ and $(1.5-2.0)\,\text{TeV}$. The first one is not only compatible with AMS-02 data, but also coincide with the non-peak excess range of DAMPE as we uncovered in Fig. 1 (the 5 red bins). The second excess is around the energy window somewhat higher than the peak excess of DAMPE (the blue bin in Fig. 1), but our fit shows
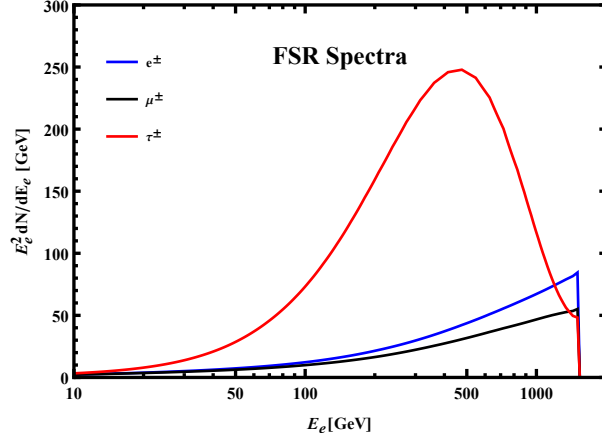
18

Figure 7: Final state radiation (FSR) spectra for $e^\pm$, $\mu^\pm$ and $\tau^\pm$ (with 1.54 TeV energy), shown as (blue, black, red) curves, respectively. The $\tau^\pm$ channel (red curve) dominates the sub-TeV region, so its fraction will be strongly constrained.

that it can match a peak structure from the DM signals with mass $M_\chi = 1.745$ TeV.

The current CRE spectra of DAMPE and CALET data show some different features, especially at energies around 1.5 TeV, which are yet to be resolved after collecting much larger data samples in the near future. But such differences are not significant given the much larger error bars of CALET data at energies above 1 TeV. Regardless of the unknown systematic effects, our above analysis still shows some compatible spectral features between these experimental data, which may be the hint of certain dark matter annihilation processes nearby and are worth of attention. Hence, the upcoming data of the on-going DAMPE and CALET measurements will be extremely helpful.

# 4. Gamma Ray Constraints from Fermi-LAT

In this section, we analyze constraints on the DM annihilation signals from the $\gamma$-ray measurements of Fermi-LAT. There have been some discussions on possible constraints from the $\gamma$-ray observations [26]. Most of the literatures assumed point-like sources of the $\gamma$-ray emission from the nearby subhalo. But such a nearby subhalo is in fact a largely extended object, so more dedicated search and analysis are necessary. The $\gamma$-rays produced by the leptons from DM annihilations consist of two main components, the prompt $\gamma$-rays and the secondary $\gamma$-rays. The former are emitted during the DM annihilations, including the final state radiation and photons from the hadronic decays of $\tau$ leptons. The latter case is the secondary emission, mainly due to the Inverse Compton Scattering (ICS) emission of electrons/positrons when propagating in the interstellar radiation field. For the nearby subhalo scenario considered in the present study, the ICS $\gamma$-rays are less than 1% and thus negligible as compared to the prompt $\gamma$-rays [26]. Thus, we will focus on the prompt $\gamma$-rays in this analysis.

| Angular Radius $\theta_0$ | 0.1° | 1.0° | 10° |
|---|---|---|---|
| Integrated $J$ Factor ($10^{20}\,\mathrm{GeV^2 cm^{-5}}$) | 2.819 | 146.5 | 3138 |
| Averaged $J$ Factor ($10^{25}\,\mathrm{GeV^2 cm^{-5} sr^{-1}}$) | 2.946 | 1.531 | 0.3288 |

Table 3: Typical values of the integrated and averaged $J$ factors.

## 4.1. Prompt Gamma Rays

We apply the PPPC4DMID code [23] to compute the energy spectra of the prompt photon emissions, as shown in Fig. 7. The $\tau^{\pm}$ channel significantly differs from that of the $e^{\pm}$ and $\mu^{\pm}$ channels, because of the $\pi^0$ products from $\tau^{\pm}$ decays. For the $e^{\pm}$ and $\mu^{\pm}$ channels, the final state radiation (FSR) comes from the internal bremsstrahlung radiation only. In Sections 2 and 3, we have determined the value of the flavor ratio $y$, which is a combination of the $\mu^{\pm}$ fraction and the $\tau^{\pm}$ fraction, through fitting to the CRE data. The $\gamma$-ray data are expected to give further constraints on the $\tau^{\pm}$ fraction due to its abundant photon production.

## 4.2. The J factor

The expected photon flux from the DM annihilations in a nearby subhalo is given by

$$\frac{\mathrm{d}^2\Phi_\gamma}{\mathrm{d}\Omega\mathrm{d}E} \;=\; \frac{J}{16\pi M_\chi^2}\sum_f \langle\sigma v\rangle_f \frac{\mathrm{d}N_f}{\mathrm{d}E}\,. \tag{4.1}$$

In the above, the $J$ factor is defined as

$$J(\theta) \;=\; \int_{\mathrm{l.o.s.}} \mathrm{d}s\,\rho_\chi^2(r)\,, \tag{4.2}$$

where $\theta$ is the angle between the line-of-sight (l.o.s.) and the subhalo center, $r$ is the radial distance from a point on l.o.s. to the subhalo center, and $s=\sqrt{r^2+d_s^2-2rd_s\cos\theta}$ is the l.o.s. distance to the observer.

For convenience, we fit the distribution of $\ln J$ as a function of $\ln\theta$, and obtain

$$\ln[J(\theta)] \;=\; C - 0.479507\ln\theta - 0.12386(\ln\theta)^2 - 0.0265383(\ln\theta)^3, \tag{4.3}$$

where $J$ is in unit of $10^{20}\,\mathrm{GeV^2 cm^{-5}}$ and $\theta$ is in unit of degrees. The constant $C$ is irrelevant here, since we are going to use a normalized skymap in the data analysis. The error of this parametrization as compared to the numerical integral of Eq.(4.2) is less than 2.5% for the angular range $\theta < 20°$.

We present in Fig. 8 the skymap of the normalized $J$ factor distribution of the subhalo in a $40°\times40°$ region, which will be used in the analysis of Fermi-LAT data in the next subsection. In Table 3, we list some typical values of the integrated $J$ factor $\int J\mathrm{d}\Omega$ in the second row and the averaged $J$ factor $\int J\mathrm{d}\Omega\,/\int\mathrm{d}\Omega$ in the third row.
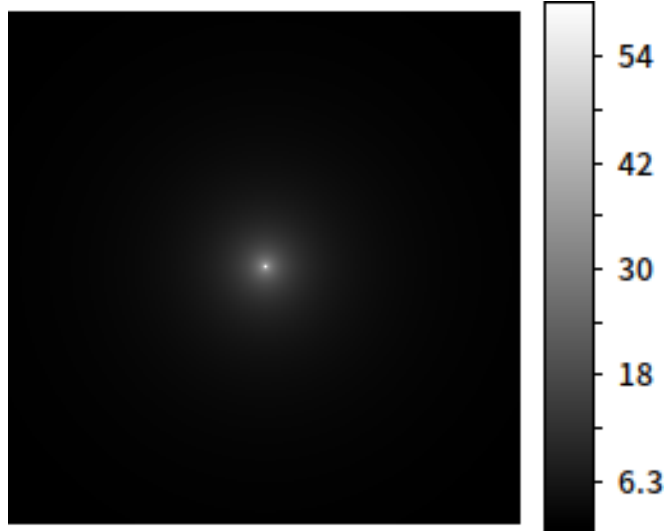
Figure 8: Skymap of the normalized $J$ factor for the DM subhalo used in our CRE fits. The vertical legend shows normalized J values with the corresponding colors in the plot.

## 4.3. Gamma Ray Searches with Fermi-LAT

We use the Pass 8 data recorded by Fermi-LAT between August 4, 2008 and July 2, 2018 to search for possible $\gamma$-ray emission from such a DM subhalo. We restrict our study with the CLEAN event class (evclass = 256 and evtype = 3). To reduce the impact from the Earth limb, the events with zenith angles $> 90°$ are excluded. We perform the searches (in a series of sky directions) within regions of interest (ROIs) centered at galactic coordinates $(\ell, b) = (0°, \pm90°)$, $(0°, \pm70°)$, $(90°, \pm70°)$, $(180°, \pm70°)$, $(270°, \pm70°)$, $(0°, 0°)$, $(0°, 30°)$, and $(120°, 45°)$, respectively. The ROI radius is chosen to be $20°$. For most of ROIs, the energy range is chosen as $100\,\mathrm{MeV}-500\,\mathrm{GeV}$. Since the expected signal appears mainly in the high energy band, we perform the analysis in the range $(1-500)\,\mathrm{GeV}$ for ROIs $(0°, 30°)$ and $(120°, 45°)$, and the range $(10-500)\,\mathrm{GeV}$ for the ROI $(0°, 0°)$, in order to speed up the analysis. For the $(0°, 0°)$ case, a higher energy threshold can also reduce the impact from the reported Galactic center GeV $\gamma$-ray excesses [27].

We use the standard binned likelihood method with the science tool version v10r0p5.[2] The model includes point sources from the 3FGL catalog [28], the diffuse background templates gll_iem_v06 and iso_P8R2_CLEAN_V6_v06,[3] as well as our postulated DM subhalo. If no clear signal is found, the 95% confidence upper limits (UL) on the annihilation cross section are derived (cf. Appendix A for detail). The mass of the DM particle is fixed to be $M_\chi = 1.54\,\mathrm{TeV}$. We study the following benchmark cases for the DM annihilation:

(a). $\langle\sigma v\rangle_e = \langle\sigma v\rangle_\mu = \langle\sigma v\rangle_\tau = 0$, which corresponds to background only;

(b). $\langle\sigma v\rangle_e = $ free, $\langle\sigma v\rangle_\mu = \langle\sigma v\rangle_\tau = 0$;

---

[2]http://fermi.gsfc.nasa.gov/ssc/data/analysis/software/
[3]http://fermi.gsfc.nasa.gov/ssc/data/access/lat/BackgroundModels.html

(c). $\langle\sigma v\rangle_\mu = \text{free}$, $\langle\sigma v\rangle_e = \langle\sigma v\rangle_\tau = 0$;

(d). $\langle\sigma v\rangle_\tau = \text{free}$, $\langle\sigma v\rangle_e = \langle\sigma v\rangle_\mu = 0$;

(e). $\langle\sigma v\rangle_e = \langle\sigma v\rangle_\mu = \langle\sigma v\rangle_\tau = \text{free}$, which corresponds to $N_e : N_\mu : N_\tau = 1 : 1 : 1$;

(f). $\langle\sigma v\rangle_e = 1.54\times 10^{-26}\text{cm}^3/\text{s}$, $\langle\sigma v\rangle_\mu = \text{free}$, $\langle\sigma v\rangle_\tau = 0$;

(g). $\langle\sigma v\rangle_e = 1.54\times 10^{-26}\text{cm}^3/\text{s}$, $\langle\sigma v\rangle_\mu = 0$, $\langle\sigma v\rangle_\tau = \text{free}$;

(h). $\langle\sigma v\rangle_e = 1.54\times 10^{-26}\text{cm}^3/\text{s}$, $\langle\sigma v\rangle_\mu = \text{free}$, $\langle\sigma v\rangle_\tau = \text{free}$;

(i). $\langle\sigma v\rangle_e = 1.54\times 10^{-26}\text{cm}^3/\text{s}$, $\langle\sigma v\rangle_\tau = \text{free}$, $\langle\sigma v\rangle_\mu = 1.39\times 10^{-25}\text{cm}^3/\text{s} - 0.178\langle\sigma v\rangle_\tau$, which corresponds to $y \equiv 9.0$.

Here the Cases (a)-(e) are generic fits, and the rest of cases are more or less motivated by our fits to the DAMPE CRE data. For illustration, we summarize the fitting results for ROIs $(0°, 30°)$ and $(90°, 70°)$ in Table 4, where we define the difference of log-likelihoods for a given Case-(j) as

$$-\Delta\ln\mathcal{L}_\text{j} = \ln[\mathcal{L}(\text{background})] - \ln[\mathcal{L}(\text{Case-j})].\tag{4.4}$$

Note that a negative value of $-\Delta\ln\mathcal{L}_\text{j}$ indicates a better fitting quality than the background-only fit (corresponding to the Case-(a)). Further discussions are given in Appendix A. The full results of all the ROIs are summarized in Appendix B.

We find that in general there lacks any DM signal from the selected ROIs. The corresponding upper limits (ULs) on the thermally averaged annihilation cross sections are derived to be about $(0.1-1)\times 10^{-25}\,\text{cm}^3\,\text{s}^{-1}$ for the $e^\pm$ and $\mu^\pm$ channels, and $1-2$ orders of magnitude stronger for $\tau^\pm$ channel. These limits depend on the directions of the sky regions which have different background intensities. The weakest constraints come from the direction towards the Galactic center region, where the backgrounds are the highest. For instance, when the DM subhalo is located at high galactic latitude such as the ROI $(90°, 70°)$, the existence of such a DM subhalo may be marginally constrained by the data. On the other hand, when the DM subhalo sits at low galactic latitudes such as the ROI $(0°, 30°)$, we see that the annihilation channels $\chi\chi \to e^+e^-, \mu^+\mu^-$ are still allowed, but as expected, the channel $\chi\chi \to \tau^+\tau^-$ is strongly constrained.

The Cases (f)-(h) which can potentially explain the peak excesses of the DAMPE measurement are generally consistent with the Fermi-LAT data. Only in a few ROIs the inclusion of such a DM component leads to slight tension with the data $(-\Delta\ln\mathcal{L} \lesssim 3.5)$. The Case-(i) is proposed to explain both the peak excess around $1.4\,\text{TeV}$ and the non-peak feature below $1\,\text{TeV}$, which can be further constrained by the Fermi-LAT data. But, when the subhalo is located in low galactic latitude regions (such as $b < 30°$), this case is also consistent with the Fermi-LAT data. Whenever $\tau^\pm$ channel is open, it is shown that the $\tau^\pm$ fraction in the DM annihilation final states is severely constrained. This also provides important guideline for the DM model building.

| $(\ell, b) = (0°, 30°)$ | | | | | | | |
|---|---|---|---|---|---|---|---|
| Case | $-\Delta\ln\mathcal{L}$ | $e^\pm$ channel | | $\mu^\pm$ channel | | $\tau^\pm$ channel | |
| | | best fit | UL | best fit | UL | best fit | UL |
| (a) | 0.00 | / | / | / | / | / | / |
| (b) | $-0.05$ | $0.16\pm0.54$ | 1.11 | / | / | / | / |
| (c) | $-0.30$ | / | / | $0.54\pm0.72$ | 1.79 | / | / |
| (d) | 0.00 | / | / | / | / | $10^{-7}$ | 0.076 |
| (e) | 0.00 | $10^{-8}$ | 0.071 | same as $e^\pm$ | | same as $e^\pm$ | |
| (f) | $-0.15$ | 0.154 | / | $0.34\pm0.72$ | 1.58 | / | / |
| (g) | $-0.05$ | 0.154 | / | / | / | $10^{-7}$ | 0.066 |
| (h) | $-0.17$ | 0.154 | / | $0.34\pm0.72$ | 1.60 | $10^{-7}$ | 0.061 |
| (i) | 0.79 | 0.154 | / | 1.39 | 1.39 | $10^{-8}$ | 0.037 |
| $(\ell, b) = (90°, 70°)$ | | | | | | | |
| Case | $-\Delta\ln\mathcal{L}$ | $e^\pm$ channel | | $\mu^\pm$ channel | | $\tau^\pm$ channel | |
| | | best fit | UL | best fit | UL | best fit | UL |
| (a) | 0.00 | / | / | / | / | / | / |
| (b) | 0.00 | $10^{-11}$ | 0.072 | / | / | / | / |
| (c) | 0.00 | / | / | $10^{-12}$ | 0.087 | / | / |
| (d) | 0.00 | / | / | / | / | $10^{-11}$ | 0.015 |
| (e) | 0.00 | $10^{-9}$ | 0.011 | same as $e^\pm$ | | same as $e^\pm$ | |
| (f) | 2.93 | 0.154 | / | $10^{-10}$ | 0.083 | / | / |
| (g) | 2.93 | 0.154 | / | / | / | $10^{-11}$ | 0.014 |
| (h) | 2.93 | 0.154 | / | $10^{-10}$ | 0.083 | $10^{-12}$ | 0.014 |
| (i) | 28.66 | 0.154 | / | 1.39 | 1.39 | $10^{-9}$ | 0.011 |

Table 4: Likelihood analysis for selected ROIs with $(\ell, b) = (0°, 30°)$ and $(90°, 70°)$. Columns from left to right correspond to the model flags, $-\Delta\ln\mathcal{L}$, the best-fit and the 95% C.L. upper limits (ULs) of the cross sections (in unit of $10^{-25}\mathrm{cm}^3\,\mathrm{s}^{-1}$) for each channel, respectively.

## 4.4. Constraints on $\tau^\pm$ Fraction

In this subsection we consider the flavor ratios $y_\mu = \langle\sigma v\rangle_\mu/\langle\sigma v\rangle_e$ and $y_\tau = 0.178\,\langle\sigma v\rangle_\tau/\langle\sigma v\rangle_e$. We scan the parameter space of the full plane of $y_\mu - y_\tau$ to further pin down the viable region for the flavor ratios in certain ROIs.

In Fig. 9(a), we plot the result in the ROI with $(\ell, b) = (0°, 30°)$. We scan the values of $(y_\mu, y_\tau)$ in the regions $y_\mu \in [0, 20]$ and $y_\tau \in [0, 0.20]$. As for the cross sections, we apply the fit relation for $y_{\mathrm{total}}$ versus $\langle\sigma v\rangle_e$ as in Fig. 3(d), rather than using the fixed value $\langle\sigma v\rangle_e = 1.54\times10^{-26}\mathrm{cm}^3/\mathrm{s}$. For the Fermi-LAT data, the $\chi^2$ function is defined as $\chi^2(y_\mu, y_\tau) = -2\ln\mathcal{L}$, and $\Delta\chi^2$ is the variation from its best fit point. In Fig. 9(a), we present the allowed regions by the $\gamma$-ray data of Fermi-LAT, in the $(y_\mu, y_\tau)$ plane at 68% (red region) and 90% (pink region) confidence limits. In the same $(y_\mu, y_\tau)$ plane, we present the DAMPE constraints from Fig. 3(b) as the blue region (light blue region) at 68% (90%) confidence limit. We see that for
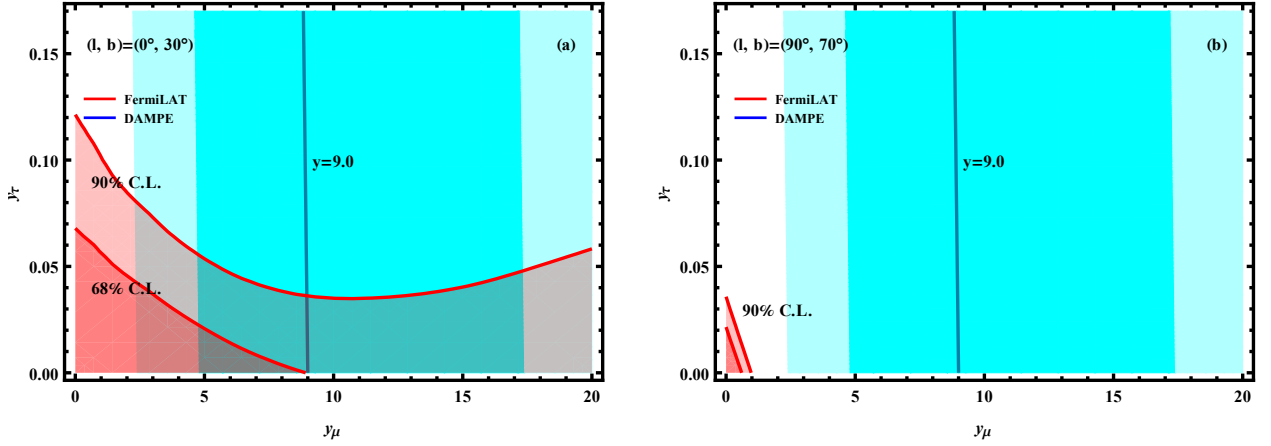
Figure 9: Allowed regions in the plane of flavor ratios $y_\mu - y_\tau$. In each plot, the red region (pink region) are allowed by the $\gamma$-ray constraints of Fermi-LAT at 68% (90%) confidence limit, while the blue region (light blue region) are allowed by the DAMPE constraints at 68% (90%) confidence limit. Plot-(a) is for the ROI centered in $(\ell, b) = (0°, 30°)$ and plot-(b) is for the ROI centered in $(\ell, b) = (90°, 70°)$.

$y_\tau = 0.035$, the case of $N_e : N_\mu : N_\tau \simeq 1 : 9.0 : 0.2$ is fully allowed at 90% C.L. in this ROI. For the lepton portal DM models discussed in Section 2.5, this corresponds to the coupling relation, $\lambda_e : \lambda_\mu : \lambda_\tau \simeq 1 : 1.7 : 0.7$.

Note that as explained in Fig. 3(d) and Section 2.4, for a large ratio $y$, the combined contribution from the $\mu^\pm$ ($\tau^\pm$) channels does not vary much as $y$ increases, but the fraction of $e^\pm$ channel will drop. Thus, the total $\gamma$-ray flux from $e^\pm$ channel will decrease, which allows more $\tau^\pm$ contribution. This is why for the 90% C.L. contour of Fermi-LAT in Fig. 9(a), the $\tau^\pm$ fraction rises up in the region of $y_\mu \gtrsim 10$. We see that in the ROI with $(\ell, b) = (0°, 30°)$, the 90% C.L. pink region allowed by the Fermi-LAT $\gamma$-ray constraint has significant overlap with that of the DAMPE CRE constraint.

For comparison, we further show the contour plot in Fig. 9(b) for the ROI with $(\ell, b) = (90°, 70°)$. It shows that in this case the Fermi-LAT $\gamma$-ray constraint is so strong that the DM subhalo scenario in this ROI is already excluded at the 90% C.L.

# 5. Conclusions

Detecting signals of TeV energy CREs has been an exciting frontier for many experimental activities in recent years [3]-[8]. These provide important means for probing the nearby galactic sources and the possible annihilations or decays of DM particles.

In Section 2, extending our previous work [16], we performed a systematically improved analysis of the DAMPE CRE data, with focus on the new hidden excess of non-peak structure over the energy range $(0.6 - 1.1)$ TeV (red bins in Fig. 1), in connection to the peak excess

around $(1.3-1.5)\,$TeV (blue bin in Fig. 1). We explain this new non-peak excess and the peak excess from the 1.5 TeV $\mu^{\pm}\,(\tau^{\pm})$ events and the 1.5 TeV $e^{\pm}$ events which are produced together from DM annihilations in a nearby subhalo, with the subsequent 3-body decays of $\mu^{\pm}\,(\tau^{\pm})$ into $e^{\pm}$ plus neutrinos (Fig. 2). We made an improved analysis of the CRE physical backgrounds which consist of CRE fluxes from SNR and ISM. Then, we systematically analyzed the CRE spectra from the DM annihilations including the final state photon radiations (which soften the CRE spectra), as shown in Fig. 2. Our improved fit analysis demonstrates that the *flavor structure* of the original lepton final-state of DM annihilations in a nearby subhalo or clump should have a flavor composition ratio $N_e : (N_\mu + 0.178 N_\tau) = 1 : y$ with $y = 9.0^{+8.4}_{-4.2}$ ($1\sigma$ bound) and $2.4 < y < 34.7$ (90% C.L.) for the current DAMPE data, as shown in Fig. 3. Using this new fit, we analyzed the lepton-portal DM models and deduced a bound on the lepton-DM-mediator couplings $\lambda_e : (\lambda_\mu^4 + \frac{1}{6}\lambda_\tau^4)^{\frac{1}{4}} = 1 : y^{\frac{1}{4}}$ with a narrow range $y^{\frac{1}{4}} \simeq 1.2 - 2.4$. Such constraints are important for DM model buildings. We further analyzed the improved sensitivities from the projected 4-year and 6-year runnings of DAMPE detector, as presented in Fig. 4. We found that assuming the current central values of the CRE spectrum, the DAMPE 6-year running will constrain the lepton flavor ratio to $y = 8.0^{+3.9}_{-3.0}$ at $1\sigma$ level and $3.4 < y < 15.7$ at 90% C.L., while the bounds from the 4-year running give $y = 8.4^{+4.6}_{-3.3}$ at $1\sigma$ level and $3.3 < y < 18.2$ at 90% C.L.

In Section 3, extending our analysis of Section 2, we further combined with the CRE measurement of Fermi-LAT [6], and then compare with the recent data from AMS-02 [5] and CALET [7]. We found that the new non-peak excess of DAMPE is consistent with the Fermi-LAT data [6]. The absence of the peak excess ($\sim 1.4\,$TeV) at Fermi-LAT may be due to its much lower energy resolution above 1 TeV scale. Our combined fit of the DAMPE and Fermi-LAT spectra is presented in Fig. 5 and constrains the flavor ratio as $y = 6.6^{+4.9}_{-2.8}$ at $1\sigma$ level and $2.2 < y < 18.1$ at 90% C.L. On the other hand, the data of AMS-02 [5] and CALET [7] show more differences from DAMPE, especially for the high energy range $E > 500\,$GeV. Nevertheless, we observe that the CALET CRE spectrum shows two broad excesses around the energy windows $(0.75 - 1.2)\,$TeV and $(1.5 - 2.0)\,$TeV, although their statistical uncertainties are still rather sizable. The first excess is compatible with the non-peak excess of DAMPE and the second excess lies at energies somewhat higher than the DAMPE peak excess. By inputting the DM mass $M_\chi = 1.78\,$TeV and using the DM cross sections from our best fit of DAMPE data, we can still fit the CALET data with good quality (Fig. 6). As compared to the pure background fit, the total $\chi^2$ only has a minor rise $\Delta\chi^2 = 1.59$.

In Section 4, we further analyzed the $\gamma$-ray measurements of Fermi-LAT and derived new constraints on the fluxes of different final state leptons from the DM annihilations. Our analysis considered for the first time the spatial extension of the $\gamma$-ray emission from the subhalo (Fig. 8). We showed in Tables 4-8 that the existence of such a nearby DM subhalo

25

at high galactic latitude is within the sensitivity reach of Fermi-LAT, although no significant $\gamma$-ray signals show up yet. For the low galactic latitude regions such as the ROI centering at $(\ell, b) = (0°, 30°)$, we found in Tables 4 and 8 that the DM annihilation channels $\chi\chi \to e^+e^-, \mu^+\mu^-$ are still viable, while the channel $\chi\chi \to \tau^+\tau^-$ is subject to a strong constraint. We presented the Fermi-LAT constraints together with the DAMPE CRE fit on the flavor ratios $(y_\mu, y_\tau)$ in Figs. 9(a) and 9(b) for two sample ROIs with low and high galactic latitudes. In the ROI centered at $(\ell, b) = (0°, 30°)$, Fig. 9(a) shows that the range of the flavor ratio $y_\tau \lesssim 0.035$ is always allowed by the Fermi-LAT $\gamma$-ray data. For instance, the flavor ratios $(y_\mu, y_\tau) = (9.0, 0.035)$ present a viable realization, which correspond to $N_e : N_\mu : N_\tau \simeq 1 : 9.0 : 0.2$ and thus the ratio of DM-lepton-mediator couplings $\lambda_e : \lambda_\mu : \lambda_\tau \simeq 1 : 1.7 : 0.7$. Such constraints give important guideline for the lepton-portal type of DM model buildings.

Our current study shows that the non-peak new excess around $(0.6 - 1.1)\,\text{TeV}$ and the tentative $1.4\,\text{TeV}$ peak structure in the DAMPE CRE spectrum provide encouraging clues to the possible new physics related to DM annihilations (decays) and the flavor composition of the final state leptons. These deserve further investigations. The future high energy CRE measurements are important to further pin down these new excesses.

## Acknowledgements

# Appendix:

# A. Likelihood and Upper Limits for the $\gamma$-Ray Analysis

The log-likelihood function of the model parameter set $\boldsymbol{p}$ is given by the Possion probability

$$\ln \mathcal{L}(\boldsymbol{p}) = \sum_j \left( n_j \ln e_j - e_j - \ln n_j! \right), \tag{A.1}$$

where $n_j$ is the observed number of photons in a given energy and spatial bin, and $e_j$ is the expected number of photons in the same bin given the model parameters. The subscript $j$ runs over all energy and spatial bins. In our analysis, the paremeter set $\boldsymbol{p}$ includes all the background parameters (i.e., spectral parameters of point sources in the ROI and the normalizations of the diffuse backgrounds), the cross section and/or the branching fraction of the DM annihilation. We adopt the profile likelihood method to deal with the background parameters [29].

In case that no signal is found, we derive the upper limits on the DM annihilation cross sections. The 95% upper limit for one-parameter fit is derived by setting $-\Delta \ln \mathcal{L} = \ln \mathcal{L}(\langle \sigma v \rangle = 0) - \ln \mathcal{L}(\langle \sigma v \rangle) < 1.35$. For the Case-(h) which has two free parameters of the DM annihilation, the 95% C.L. upper limit is defined by $-\Delta \ln \mathcal{L} < 2.30$.

# B. Summary of $\gamma$-ray Fitting Results for All ROIs

In this Appendix, we summarize the fitting results in all ROIs, in addition to Table 4 as presented in Section 4.3. In each table, the columns from left to right correspond to the model flags, $-\Delta \ln \mathcal{L}$, best-fit and 95% upper limit (UL) of the cross sections (in units of $10^{-25} \mathrm{cm}^3 \, \mathrm{s}^{-1}$) for each channel.

From Tables 5-7, we see that at high latitudes with $b \geqslant 70°$, the Fermi-LAT $\gamma$-ray data not only show null results for the DM annihilation signal at its best fits, but also exclude our model motivated by the DAMPE data at 95% C.L.

On the other hand, in the ROIs at low latitudes with $b \leqslant 30°$, we find that our proposed DM subhalo is allowed by the constraints of the 10-year $\gamma$-ray data from Fermi-LAT experiment, although no significant signals show up yet. But in this case, we can derive an upper bound on the flavor ratio of $\tau^{\pm}$. We present this analysis in Table 4 (Section 4.3) and the following Table 8.

| Case | $-\Delta\ln\mathcal{L}$ | $e^{\pm}$ channel | | $\mu^{\pm}$ channel | | $\tau^{\pm}$ channel | |
|---|---|---|---|---|---|---|---|
| | | best fit | UL | best fit | UL | best fit | UL |
| $(\ell,\ b) = (0°,\ 90°)$ | | | | | | | |
| (a) | 0.00 | / | / | / | / | / | / |
| (b) | 0.00 | $10^{-6}$ | 0.143 | / | / | / | / |
| (c) | 0.00 | / | / | $10^{-6}$ | 0.160 | / | / |
| (d) | 0.00 | / | / | / | / | $10^{-6}$ | 0.037 |
| (e) | 0.00 | $10^{-6}$ | 0.025 | same as $e^{\pm}$ | | same as $e^{\pm}$ | |
| (f) | 1.46 | 0.154 | / | $10^{-6}$ | 0.133 | / | / |
| (g) | 1.46 | 0.154 | / | / | / | $10^{-7}$ | 0.028 |
| (h) | 1.46 | 0.154 | / | $10^{-6}$ | 0.133 | $10^{-7}$ | 0.028 |
| (i) | 20.52 | 0.154 | / | 1.39 | 1.39 | $10^{-7}$ | 0.015 |
| $(\ell,\ b) = (0°,\ -90°)$ | | | | | | | |
| (a) | 0.00 | / | / | / | / | / | / |
| (b) | 0.00 | $10^{-6}$ | 0.093 | / | / | / | / |
| (c) | 0.00 | / | / | $10^{-6}$ | 0.108 | / | / |
| (d) | 0.00 | / | / | / | / | $10^{-6}$ | 0.011 |
| (e) | 0.00 | $10^{-6}$ | 0.016 | same as $e^{\pm}$ | | same as $e^{\pm}$ | |
| (f) | 2.27 | 0.154 | / | $10^{-6}$ | 0.101 | / | / |
| (g) | 2.27 | 0.154 | / | / | / | $10^{-7}$ | 0.021 |
| (h) | 2.27 | 0.154 | / | $10^{-6}$ | 0.100 | $10^{-7}$ | 0.021 |
| (i) | 24.31 | 0.154 | / | 1.39 | 1.39 | $10^{-7}$ | 0.014 |

Table 5: The likelihood analysis for ROIs centered at the north and south Galactic poles. Columns from left to right correspond to the model flags, $-\Delta\ln\mathcal{L}$, best-fit, and 95% confidence upper limits (UL) of the cross sections (in unit of $10^{-25}\mathrm{cm}^3\mathrm{s}^{-1}$) for each channel, respectively.

| Case | $-\Delta\ln\mathcal{L}$ | $e^\pm$ channel | | $\mu^\pm$ channel | | $\tau^\pm$ channel | |
|---|---|---|---|---|---|---|---|
| | | best fit | UL | best fit | UL | best fit | UL |
| $(\ell, b) = (0°, 70°)$ | | | | | | | |
| (a) | 0.00 | / | / | / | / | / | / |
| (b) | 0.00 | $10^{-11}$ | 0.066 | / | / | / | / |
| (c) | 0.00 | / | / | $10^{-7}$ | 0.080 | / | / |
| (d) | 0.00 | / | / | / | / | $10^{-9}$ | 0.013 |
| (e) | 0.00 | $10^{-11}$ | 0.010 | same as $e^\pm$ | | same as $e^\pm$ | |
| (f) | 3.18 | 0.154 | / | $10^{-8}$ | 0.077 | / | / |
| (g) | 3.18 | 0.154 | / | / | / | $10^{-9}$ | 0.012 |
| (h) | 3.18 | 0.154 | / | $10^{-8}$ | 0.077 | $10^{-9}$ | 0.012 |
| (i) | 30.08 | 0.154 | / | 1.39 | 1.39 | $10^{-10}$ | 0.011 |
| $(\ell, b) = (90°, 70°)$ | | | | | | | |
| (a) | 0.00 | / | / | / | / | / | / |
| (b) | 0.00 | $10^{-11}$ | 0.072 | / | / | / | / |
| (c) | 0.00 | / | / | $10^{-12}$ | 0.087 | / | / |
| (d) | 0.00 | / | / | / | / | $10^{-11}$ | 0.015 |
| (e) | 0.00 | $10^{-9}$ | 0.011 | same as $e^\pm$ | | same as $e^\pm$ | |
| (f) | 2.93 | 0.154 | / | $10^{-10}$ | 0.083 | / | / |
| (g) | 2.93 | 0.154 | / | / | / | $10^{-11}$ | 0.014 |
| (h) | 2.93 | 0.154 | / | $10^{-10}$ | 0.083 | $10^{-12}$ | 0.014 |
| (i) | 28.66 | 0.154 | / | 1.39 | 1.39 | $10^{-9}$ | 0.011 |
| $(\ell, b) = (180°, 70°)$ | | | | | | | |
| (a) | 0.00 | / | / | / | / | / | / |
| (b) | 0.00 | $10^{-6}$ | 0.085 | / | / | / | / |
| (c) | 0.00 | / | / | $10^{-6}$ | 0.102 | / | / |
| (d) | 0.00 | / | / | / | / | $10^{-6}$ | 0.018 |
| (e) | 0.00 | $10^{-6}$ | 0.018 | same as $e^\pm$ | | same as $e^\pm$ | |
| (f) | 2.48 | 0.154 | / | $10^{-6}$ | 0.096 | / | / |
| (g) | 2.48 | 0.154 | / | / | / | $10^{-7}$ | 0.016 |
| (h) | 2.48 | 0.154 | / | $10^{-6}$ | 0.096 | $10^{-7}$ | 0.016 |
| (i) | 24.98 | 0.154 | / | 1.39 | 1.39 | $10^{-7}$ | 0.013 |
| $(\ell, b) = (270°, 70°)$ | | | | | | | |
| (a) | 0.00 | / | / | / | / | / | / |
| (b) | 0.00 | $10^{-6}$ | 0.083 | / | / | / | / |
| (c) | 0.00 | / | / | $10^{-6}$ | 0.094 | / | / |
| (d) | 0.00 | / | / | / | / | $10^{-6}$ | 0.021 |
| (e) | 0.00 | $10^{-6}$ | 0.015 | same as $e^\pm$ | | same as $e^\pm$ | |
| (f) | 2.55 | 0.154 | / | $10^{-6}$ | 0.088 | / | / |
| (g) | 2.55 | 0.154 | / | / | / | $10^{-6}$ | 0.019 |
| (h) | 2.55 | 0.154 | / | $10^{-6}$ | 0.088 | $10^{-6}$ | 0.019 |
| (i) | 27.31 | 0.154 | / | 1.39 | 1.39 | $10^{-6}$ | 0.014 |

Table 6: The likelihood analysis for ROIs at high latitudes with $b = 70°$. All the notations are the same as in Table 5.

| Case | $-\Delta\ln\mathcal{L}$ | $e^\pm$ channel | | $\mu^\pm$ channel | | $\tau^\pm$ channel | |
|---|---|---|---|---|---|---|---|
| | | best fit | UL | best fit | UL | best fit | UL |
| $(\ell, b) = (0^\circ, -70^\circ)$ | | | | | | | |
| (a) | 0.00 | / | / | / | / | / | / |
| (b) | 0.00 | $10^{-11}$ | 0.156 | / | / | / | / |
| (c) | 0.00 | / | / | $10^{-11}$ | 0.197 | / | / |
| (d) | 0.00 | / | / | / | / | $10^{-12}$ | 0.028 |
| (e) | 0.00 | $10^{-13}$ | 0.021 | same as $e^\pm$ | | same as $e^\pm$ | |
| (f) | 1.33 | 0.154 | / | $10^{-10}$ | 0.177 | / | / |
| (g) | 1.33 | 0.154 | / | / | / | $10^{-13}$ | 0.025 |
| (h) | 1.33 | 0.154 | / | $10^{-10}$ | 0.177 | $10^{-11}$ | 0.025 |
| (i) | 15.00 | 0.154 | / | 1.39 | 1.39 | $10^{-12}$ | 0.017 |
| $(\ell, b) = (90^\circ, -70^\circ)$ | | | | | | | |
| (a) | 0.00 | / | / | / | / | / | / |
| (b) | 0.00 | $10^{-8}$ | 0.106 | / | / | / | / |
| (c) | 0.00 | / | / | $10^{-9}$ | 0.117 | / | / |
| (d) | 0.00 | / | / | / | / | $10^{-10}$ | 0.032 |
| (e) | 0.00 | $10^{-9}$ | 0.020 | same as $e^\pm$ | | same as $e^\pm$ | |
| (f) | 1.99 | 0.154 | / | $10^{-8}$ | 0.109 | / | / |
| (g) | 1.99 | 0.154 | / | / | / | $10^{-10}$ | 0.028 |
| (h) | 1.99 | 0.154 | / | $10^{-8}$ | 0.109 | $10^{-11}$ | 0.028 |
| (i) | 22.69 | 0.154 | / | 1.39 | 1.39 | $10^{-9}$ | 0.017 |
| $(\ell, b) = (180^\circ, -70^\circ)$ | | | | | | | |
| (a) | 0.00 | / | / | / | / | / | / |
| (b) | 0.00 | $10^{-6}$ | 0.106 | / | / | / | / |
| (c) | 0.00 | / | / | $10^{-6}$ | 0.122 | / | / |
| (d) | 0.00 | / | / | / | / | $10^{-12}$ | 0.029 |
| (e) | 0.00 | $10^{-9}$ | 0.019 | same as $e^\pm$ | | same as $e^\pm$ | |
| (f) | 1.99 | 0.154 | / | $10^{-7}$ | 0.112 | / | / |
| (g) | 1.99 | 0.154 | / | / | / | $10^{-10}$ | 0.025 |
| (h) | 1.99 | 0.154 | / | $10^{-7}$ | 0.112 | $10^{-10}$ | 0.025 |
| (i) | 22.41 | 0.154 | / | 1.39 | 1.39 | $10^{-10}$ | 0.016 |
| $(\ell, b) = (270^\circ, -70^\circ)$ | | | | | | | |
| (a) | 0.00 | / | / | / | / | / | / |
| (b) | 0.00 | $10^{-7}$ | 0.209 | / | / | / | / |
| (c) | 0.00 | / | / | $10^{-7}$ | 0.243 | / | / |
| (d) | 0.00 | / | / | / | / | $10^{-13}$ | 0.054 |
| (e) | 0.00 | $10^{-9}$ | 0.037 | same as $e^\pm$ | | same as $e^\pm$ | |
| (f) | 0.92 | 0.154 | / | $10^{-7}$ | 0.194 | / | / |
| (g) | 0.92 | 0.154 | / | / | / | $10^{-10}$ | 0.040 |
| (h) | 0.92 | 0.154 | / | $10^{-7}$ | 0.194 | $10^{-7}$ | 0.040 |
| (i) | 41.08 | 0.154 | / | 1.39 | 1.39 | $10^{-13}$ | 0.013 |

Table 7: The likelihood analysis for ROIs at high latitutes with $b = -70^\circ$. All the notations are the same as in Table 5.

| Case | $-\Delta\ln\mathcal{L}$ | $e^{\pm}$ channel | | $\mu^{\pm}$ channel | | $\tau^{\pm}$ channel | |
|---|---|---|---|---|---|---|---|
| | | best fit | UL | best fit | UL | best fit | UL |
| $(\ell,\,b)=(120°,45°)$ | | | | | | | |
| (a) | 0.00 | / | / | / | / | / | / |
| (b) | $-0.39$ | $0.16\pm0.20$ | 0.541 | / | / | / | / |
| (c) | $-0.31$ | / | / | $0.18\pm0.25$ | 0.663 | / | / |
| (d) | $-0.42$ | / | / | / | / | $0.024\pm0.030$ | 0.083 |
| (e) | $-0.41$ | $0.019\pm0.024$ | 0.065 | same as $e^{\pm}$ | | same as $e^{\pm}$ | |
| (f) | $-0.39$ | 0.154 | / | $10^{-6}$ | 0.464 | / | / |
| (g) | $-0.39$ | 0.154 | / | / | / | $10^{-4}$ | 0.061 |
| (h) | $-0.39$ | 0.154 | / | $10^{-6}$ | 0.443 | $10^{-4}$ | 0.061 |
| (i) | 8.79 | 0.154 | / | 1.39 | 1.39 | $10^{-9}$ | 0.018 |
| $(\ell,\,b)=(0°,30°)$ | | | | | | | |
| (a) | 0.00 | / | / | / | / | / | / |
| (b) | $-0.05$ | $0.16\pm0.54$ | 1.11 | / | / | / | / |
| (c) | $-0.30$ | / | / | $0.54\pm0.72$ | 1.79 | / | / |
| (d) | 0.00 | / | / | / | / | $10^{-7}$ | 0.076 |
| (e) | 0.00 | $10^{-8}$ | 0.071 | same as $e^{\pm}$ | | same as $e^{\pm}$ | |
| (f) | $-0.15$ | 0.154 | / | $0.34\pm0.72$ | 1.58 | / | / |
| (g) | $-0.05$ | 0.154 | / | / | / | $10^{-7}$ | 0.066 |
| (h) | $-0.17$ | 0.154 | / | $0.34\pm0.72$ | 1.60 | $10^{-7}$ | 0.061 |
| (i) | 0.79 | 0.154 | / | 1.39 | 1.39 | $10^{-8}$ | 0.037 |
| $(\ell,\,b)=(0°,0°)$ | | | | | | | |
| (a) | 0.00 | / | / | / | / | / | / |
| (b) | 0.00 | $10^{-7}$ | 0.803 | / | / | / | / |
| (c) | 0.18 | / | / | $10^{-7}$ | 1.15 | / | / |
| (d) | 0.00 | / | / | / | / | $10^{-9}$ | 0.117 |
| (e) | 0.16 | $10^{-7}$ | 0.095 | same as $e^{\pm}$ | | same as $e^{\pm}$ | |
| (f) | 0.26 | 0.154 | / | $10^{-7}$ | 1.00 | / | / |
| (g) | 0.27 | 0.154 | / | / | / | $10^{-11}$ | 0.113 |
| (h) | 0.26 | 0.154 | / | $10^{-7}$ | 1.01 | $10^{-4}$ | 0.113 |
| (i) | 2.20 | 0.154 | / | 1.39 | 1.39 | $10^{-10}$ | 0.089 |

Table 8: The likelihood analysis for ROIs at medium and low Galactic latitudes. All the notations are the same as in Table 5. As mentioned in Section 4.3, here the photon energy range for the region $(0°,\,30°)$ is chosen to be $(10-500)\,\mathrm{GeV}$, instead of the range $(1-500)\,\mathrm{GeV}$ in other regions.

# References

[1] P. Meyer, *"Cosmic rays in the galaxy"*, Ann. Rev. Astron. Astrophys. 7 (1969) 1; C. S. Shen, *"Pulsars and very high-energy cosmic-ray electrons"*, Astrophys. J. 162 (1970) L181; T. Kobayashi, Y. Komori, K. Yoshida and J. Nishimura, *"The most likely sources of high energy cosmic-ray electrons in supernova remnants"*, Astrophys. J. 601 (2004) 340 [arXiv:astro-ph/0308470]; Y. Z. Fan, B. Zhang and J. Chang, *"$e^{\pm}$ Excesses in the Cosmic Ray Spectrum and Possible Interpretations"*, Int. J. Mod. Phys. D 19 (2010) 2011, [arXiv:1008.4646 [astro-ph.HE]].

[2] M. S. Turner and F. Wilczek, *"Positron Line Radiation from Halo WIMP Annihilations as a Dark Matter Signature"*, Phys. Rev. D 42 (1990) 1001; G. Bertone, D. Hooper and J. Silk, *"Particle dark matter: Evidence, candidates and constraints"*, Phys. Rept. 405 (2005) 279 [arXiv:hep-ph/0404175]; J. L. Feng, *"Dark Matter Candidates from Particle Physics and Methods of Detection"*, Ann. Rev. Astron. Astrophys. 48 (2010) 495 [arXiv:1003.0904 [astro-ph.CO]].

[3] F. Aharonian *et al.* [HESS Collaboration], *"The energy spectrum of cosmic-ray electrons at TeV energies"*, Phys. Rev. Lett. 101 (2008) 261104 [arXiv:0811.3894 [astro-ph]]; *"Probing the ATIC peak in the cosmic-ray electron spectrum with HESS"*, Astron. Astrophys. 508 (2009) 561 [arXiv:0905.0105 [astro-ph.HE]]; P. Brun, *"Particle Physics and Cosmology with H.E.S.S."*, Nucl. Part. Phys. Proc. 291-293 (2017) 25.

[4] J. Holder [for VERITAS Collaboration], *"Latest Results from VERITAS: Gamma 2016"*, AIP Conf. Proc. 1792 (2017) 020013 [arXiv:1609.02881 [astro-ph.HE]]; D. Staszak [for VERITAS Collaboration], *"A Cosmic-ray Electron Spectrum with VERITAS"*, PoS ICRC 2015 (2016) 411 [arXiv:1508.06597 [astro-ph.HE]]; *"Science Highlights from VERITAS"*, PoS ICRC 2015 (2016) 868 [arXiv:1510.01269 [astro-ph.HE]].

[5] M. Aguilar *et al.* [AMS Collaboration], "Towards Understanding the Origin of Cosmic-Ray Electrons", Phys. Rev. Lett. 122 (2019) 101101, no.10; and *"Towards Understanding the Origin of Cosmic-Ray Positrons"*, Phys. Rev. Lett. 122 (2019) 041102, no.4.

[6] S. Abdollahi *et al.* [Fermi-LAT Collaboration], *"Cosmic-ray electron-positron spectrum from 7GeV to 2TeV with the Fermi Large Area Telescope"*, Phys. Rev. D 95 (2017) 082007 [arXiv:1704.07195 [astro-ph.HE]]; M. Meehan *et al.* [Fermi-LAT Collaboration], *"A Search for Cosmic-ray Proton Anisotropy with the Fermi Large Area Telescope"*, PoS ICRC 2017 (2018) 170 [arXiv:1708.07796 [astro-ph.HE]].

[7] O. Adriani *et al.* [CALET Collaboration], *"Energy Spectrum of Cosmic-Ray Electron and Positron from 10GeV to 3TeV Observed with the Calorimetric Electron Telescope on the International Space Station,"* Phys. Rev. Lett. 119 (2017) 181101 [arXiv:1712.01711 [astro-ph.HE]]; and *"Extended Measurement of the Cosmic-Ray Electron and Positron*

*Spectrum from 11GeV to 4.8TeV with the Calorimetric Electron Telescope on the International Space Station*", Phys. Rev. Lett. 120 (2018) 261102 [arXiv:1806.09728 [astro-ph.HE]].

[8] G. Ambrosi *et al.* [DAMPE Collaboration], *"Direct detection of a break in the teraelectronvolt cosmic-ray spectrum of electrons and positrons,"* Nature 552 (2017) 63 [arXiv:1711.10981 [astro-ph.HE]].

[9] J. Chang, *"Dark Matter Particle Explorer: The First Chinese Cosmic Ray and Hard Gamma-ray Detector in Space"*, Chinese Journal of Space Science 34 (2014) 550; J. Chang *et al.* [DAMPE Collaboration], *"The DArk Matter Particle Explorer mission,"* Astropart. Phys. 95 (2017) 6 [arXiv:1706.08453 [astro-ph.IM]].

[10] Q. Yuan *et al.*, *"Interpretations of the DAMPE electron data,"* [arXiv:1711.10989 [astro-ph.HE]].

[11] K. Fang, X. J. Bi and P. F. Yin, *"Explanation of the knee-like feature in the DAMPE cosmic $e^- + e^+$ energy spectrum,"* Astrophys. J. 854 (2018) 57 [arXiv:1711.10996 [astro-ph.HE]];

[12] X. J. Huang, Y. L. Wu, W. H. Zhang and Y. F. Zhou, *"Origins of sharp cosmic-ray electron structures and the DAMPE excess,"* Phys. Rev. D 97 (2018) 091701 [arXiv:1712.00005 [astro-ph.HE]];

[13] H. B. Jin, B. Yue, X. Zhang and X. Chen, *"Cosmic ray $e^+e^-$ spectrum excess and peak feature observed by the DAMPE experiment from dark matter,"* Phys. Rev. D 98 (2018) 123008 [arXiv:1712.00362 [astro-ph.HE]];

[14] Y. Gao and Y. Z. Ma, *"Implications of dark matter cascade decay from DAMPE, HESS, Fermi-LAT and AMS02 data,"* Mon. Not. Roy. Astron. Soc. 491 (2020) 965 [arXiv:1712.00370 [astro-ph.HE]];

[15] F. Yang, M. Su and Y. Zhao, *"Dark Matter Annihilation from Nearby Ultra-compact Micro Halos to Explain the Tentative Excess at  1.4 TeV in DAMPE data,"* [arXiv:1712.01724 [astro-ph.HE]]; Y. Zhao, K. Fang, M. Su and M. C. Miller, *"A strong test of the dark matter origin of a TeV electron excess using icecube neutrinos,"* JCAP 1806 (2018) 030 [arXiv:1712.03210 [astro-ph.HE]].

[16] S. F. Ge, H. J. He, and Y. C. Wang, *"Flavor Structure of the Cosmic-Ray Electron/ Positron Excesses at DAMPE"*, Phys. Lett. B 781 (2018) 88 [arXiv:1712.02744 [astro-ph.HE]].

[17] Y. Z. Fan, W. C. Huang, M. Spinrath, Y. L. S. Tsai and Q. Yuan, Phys. Lett. B 781 (2018) 83 [arXiv:1711.10995 [hep-ph]]; P. H. Gu and X. G. He, Phys. Lett. B

778 (2018) 292 [arXiv:1711.11000 [hep-ph]]; G. H. Duan, L. Feng, F. Wang, L. Wu, J. M. Yang and R. Zheng, JHEP 1802 (2018) 107 [arXiv:1711.11012 [hep-ph]]; Y. L. Tang, L. Wu, M. Zhang and R. Zheng, Sci. China Phys. Mech. Astron. 61 (2018) 101003 [arXiv:1711.11058 [hep-ph]]; L. Zu, C. Zhang, L. Feng, Q. Yuan and Y. Z. Fan, Phys. Rev. D 98 (2018) 063010 [arXiv:1711.11052 [hep-ph]]; W. Chao and Q. Yuan, arXiv:1711.11182 [hep-ph]; P. Athron, C. Balazs, A. Fowlie and Y. Zhang, JHEP 1802 (2018) 121 [arXiv:1711.11376 [hep-ph]]; J. Cao, L. Feng, X. Guo, L. Shang, F. Wang and P. Wu, Phys. Rev. D 97 (2018) 095011 [arXiv:1711.11452 [hep-ph]]; X. Liu and Z. Liu, Phys. Rev. D 98 (2018) 035025 [arXiv:1711.11579 [hep-ph]]; G. H. Duan, X. G. He, L. Wu and J. M. Yang, Eur. Phys. J. C 78 (2018) 323 [arXiv:1711.11563 [hep-ph]]; J. S. Niu, T. Li, R. Ding, B. Zhu, H. F. Xue and Y. Wang, Phys. Rev. D 97 (2018) 083012 [arXiv:1712.00372 [astro-ph.HE]]; W. Chao, H. K. Guo, H. L. Li and J. Shu, Phys. Lett. B 782 (2018) 517 [arXiv:1712.00037 [hep-ph]]; C. H. Chen, C. W. Chiang and T. Nomura, Phys. Rev. D 97 (2018) 061302 [arXiv:1712.00793 [hep-ph]]; T. Li, N. Okada and Q. Shafi, Phys. Lett. B 779 (2018) 130 [arXiv:1712.00869 [hep-ph]]; R. Zhu and Y. Zhang, arXiv:1712.01143 [hep-ph]; T. Nomura and H. Okada, Phys. Dark Univ. 21 (2018) 90 [arXiv:1712.00941 [hep-ph]]; K. Ghorbani and P. H. Ghorbani, JHEP 1805 (2018) 125 [arXiv:1712.01239 [hep-ph]]; J. Cao, L. Feng, X. Guo, L. Shang, F. Wang, P. Wu and L. Zu, Eur. Phys. J. C 78 (2018) 198 [arXiv:1712.01244 [hep-ph]]; R. Ding, Z. L. Han, L. Feng and B. Zhu, Chin. Phys. C 42 (2018) 083104 [arXiv:1712.02021 [hep-ph]]; B. Wang, X. Bi, S. Lin and P. Yin, Sci. China Phys. Mech. Astron. 61 (2018) 101004; X. Pan, C. Zhang and L. Feng, Sci. China Phys. Mech. Astron. 61 (2018) 101006; F. Elahi and S. Khatibi, Phys. Rev. D 100 (2019) 015019 [arXiv:1902.04384 [hep-ph]]; X. Liu, Z. Liu and Y. Su, JHEP 1906 (2019) 109 [arXiv:1902.04916 [hep-ph]]; L. Feng, Z. Kang, Q. Yuan, P. F. Yin, Y. Z. Fan, arXiv:1902.09235 [hep-ph]; M. H. Chan and C. M. Lee, Mon. Not. Roy. Astron. Soc. 486 (2019) L85 [arXiv:1904.12418 [astro-ph.HE]]; C. Q. Geng, D. Huang and L. Yin, [arXiv:1905.10136 [hep-ph]]; Y. Zhao, X. J. Bi, S. J. Lin and P. F. Yin, Chin. Phys. C 43 (2019) 085101; S. Yaser Ayazi and A. Mohamadnejad, arXiv:1909.10729 [hep-ph].

[18] For a review, Q. Yuan and L. Feng, "*Dark Matter Particle Explorer observations of high-energy cosmic ray electrons plus positrons and their physical implications*", Sci. China Phys. Mech. Astron. 61 (2018) 101002 [arXiv:1807.11638 [astro-ph.HE]].

[19] J. F. Navarro, C. S. Frenk and S. D. M. White, "*A Universal density profile from hierarchical clustering*", Astrophys. J. 490 (1997) 493 [astro-ph/9611107].

[20] M. Tanabashi *et al.,* [Particle Data Group], Phys. Rev. D 98 (2018) 030001.

[21] Y. Bai and J. Berger, "*Lepton Portal Dark Matter*", JHEP 1408 (2014) 153 [arXiv:1402.6696 [hep-ph]].

[22] X. Huang, Y. L. S. Tsai and Q. Yuan, "*LikeDM: likelihood calculator of dark matter detection*", Comput. Phys. Commun. 213 (2017) 252 [arXiv:1603.07119 [hep-ph]].

[23] M. Cirelli *et al.*, "*PPPC 4 DM ID: A Poor Particle Physicist Cookbook for Dark Matter Indirect Detection*", JCAP 1103 (2011) 051, Erratum: JCAP 1210 (2012) E01 [arXiv:1012.4515 [hep-ph]].

[24] P. Ciafaloni, D. Comelli, A. Riotto, F. Sala, A. Strumia and A. Urbano, "*Weak Corrections are Relevant for Dark Matter Indirect Detection*", JCAP 1103 (2011) 019 [arXiv:1009.0224 [hep-ph]].

[25] M. Kuhlen and D. Malyshev, "*ATIC, PAMELA, HESS, Fermi and nearby Dark Matter subhalos*", Phys. Rev. D 79 (2009) 123517 [arXiv:0904.3378 [hep-ph]]; T. Delahaye, J. Lavalle, R. Lineros, F. Donato and N. Fornengo, "*Galactic electrons and positrons at the Earth:new estimate of the primary and secondary fluxes*", Astron. Astrophys. 524 (2010) A51 [arXiv:1002.1910 [astro-ph.HE]].

[26] T. Ghosh, J. Kumar, D. Marfatia and P. Sandick, "*Searching for light from a dark matter clump*", JCAP 1808 (2018) 023 [arXiv:1804.05792 [astro-ph.HE]]; A. Coogan, B. V. Lehmann and S. Profumo, "*Connecting direct and indirect detection with a dark spike in the cosmic-ray electron spectrum,*" JCAP 1910 (2019) 063 [arXiv:1903.07177 [astro-ph.HE]]. K. Belotsky, A. Kamaletdinov, M. Laletin and M. Solovyov, "*The DAMPE excess and gamma-ray constraints,*" Phys. Dark Univ. 26 (2019) 100333 [arXiv:1904.02456 [astro-ph.HE]];

[27] D. Hooper and L. Goodenough, "*Dark Matter Annihilation in The Galactic Center As Seen by the Fermi Gamma Ray Space Telescope,*" Phys. Lett. B 697 (2011) 412 [arXiv:1010.2752 [hep-ph]]; T. Daylan, D. P. Finkbeiner, D. Hooper, T. Linden, S. K. N. Portillo, N. L. Rodd and T. R. Slatyer, "*The characterization of the gamma-ray signal from the central Milky Way: A case for annihilating dark matter,*" Phys. Dark Univ. 12 (2016) 1 [arXiv:1402.6703 [astro-ph.HE]].

[28] F. Acero *et al.* [Fermi-LAT Collaboration], "*Fermi Large Area Telescope Third Source Catalog,*" Astrophys. J. Suppl. 218 (2015) 23 [arXiv:1501.02003 [astro-ph.HE]].

[29] W. A. Rolke, A. M. Lopez and J. Conrad, "*Limits and confidence intervals in the presence of nuisance parameters,*" Nucl. Instrum. Meth. A 551 (2005) 493 [physics/0403059].